SIAM J. IMAGING SCIENCES
Vol. 8, No. 4, pp. 2683–2705

Passive Synthetic Aperture Imaging*

Josselin Garnier† and George Papanicolaou‡

Abstract. We consider passive synthetic aperture imaging where a single moving receiver antenna records signals that are generated by distant unknown noise sources and backscattered by one or several reflectors. The reflectors can be imaged by migrating the autocorrelation functions of the received signals. We compare this passive synthetic aperture imaging with the usual, active synthetic aperture imaging. In the usual synthetic aperture imaging the moving receiver antenna is also a transmitter, and imaging is done by application of a matched filter to the recorded signals. We show that image resolution is the same in both active and passive synthetic aperture imaging, provided that the illumination in the passive case is rich enough.

Key words. imaging, wave propagation, synthetic aperture radar, correlation, noise sources

AMS subject classifications. 78A46, 35R60, 35Q60

DOI. 10.1137/15M1019696

1. Introduction.

We consider passive synthetic aperture (PSA) imaging where a single moving receiver antenna records signals that are generated by distant unknown noise sources and backscattered by one or several reflectors (see Figure 1). We will show that the reflectors can be imaged by migrating the autocorrelation functions of the received signals.

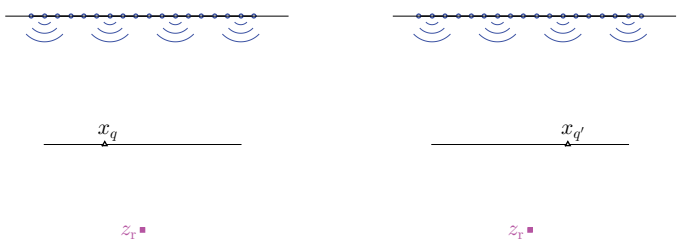

Figure 1. *A PSA imaging configuration. Two positions $\boldsymbol{x}_q$ and $\boldsymbol{x}_{q'}$ of the moving receiver antenna are plotted. The circles are the noise sources. The square is a reflector at $\boldsymbol{z}_r$.*

Passive synthetic aperture imaging is of interest for several fields of applications. In passive underwater acoustics, one may want to use exploration robots or unmanned underwater vehicles to look for mines or submarines in a passive mode by using only the ambient noise signals generated by opportunistic sources, located mainly at the surface [19, 23]. In radar

*Received by the editors May 4, 2015; accepted for publication (in revised form) September 14, 2015; published electronically November 24, 2015.
http://www.siam.org/journals/siims/8-4/M101969.html
†Laboratoire de Probabilités et Modèles Aléatoires & Laboratoire Jacques-Louis Lions, Université Paris Diderot, 75205 Paris Cedex 13, France (garnier@math.univ-paris-diderot.fr).
‡Department of Mathematics, Stanford University, Stanford, CA 94305 (papanicolaou@stanford.edu). The work of this author was supported by AFOSR grant FA9550-14-1-0275.

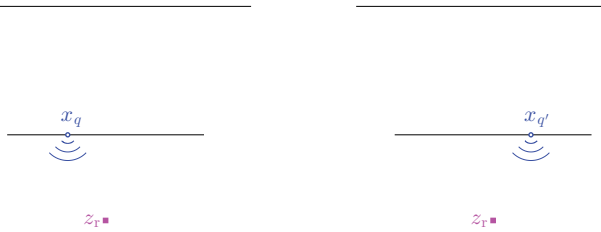

Figure 2. *An active synthetic aperture imaging configuration. Two positions $\boldsymbol{x}_q$ and $\boldsymbol{x}_{q'}$ of the moving source-receiver antenna are plotted. $\boldsymbol{z}_r$ is a reflector.*

imaging the papers in the special issue [11] discuss the need for passive imaging techniques using only a receiver antenna and unknown, uncontrolled, asynchronous, and/or opportunistic sources. These sources could be a collection of satellites, and the receiver antenna could be on a low flying platform. It is pointed out in [11] that the recent interest in passive radar techniques is due to (i) the increased demand for affordable and environmentally friendly monitoring systems and (ii) the reduction of the electromagnetic spectrum available for radar applications due to the increased demand for wideband mobile communication systems. Passive radar systems that can operate by using opportunistic sources are strong candidates for addressing these challenges.

The main objective of this paper is to compare the PSA images obtained by migration of the autocorrelation functions with the usual, active synthetic aperture images. In usual synthetic aperture imaging [7] the moving receiver antenna is also a transmitter (see Figure 2), and imaging is done by application of a matched filter to the recorded signals. We describe the two imaging configurations in sections 2 and 4, respectively. We show that image resolution in the active and passive configurations is the same, provided that the illumination in the passive case is rich enough. This is the main result of the paper. The analysis is in a high-frequency regime and is carried out in section 3. We also explain in section 5 that PSA imaging can be given a time-reversal interpretation [9, 10, 18] and that it is related to another correlation-based imaging technique, called virtual source imaging, that is used in seismic exploration [1, 6, 24, 26]. These remarks help clarify the relation between time-reversal and active and passive migration imaging. We provide some numerical illustrations of the main results in section 6.

2. Passive synthetic aperture imaging.

2.1. Passive synthetic aperture imaging setup. Throughout this paper the spatial variable is written $\boldsymbol{x} = (\boldsymbol{x}_\perp, z) \in \mathbb{R}^2 \times \mathbb{R}$. In this section we assume that there is a noise source distribution in the plane $z = 0$, a single moving receiver antenna in the plane $z = -L$, and a reflector in the plane $z = -L_r$, with $-L_r < -L < 0$ (see Figure 3). The reflector is modeled by a local change of the speed of propagation of the form

$$\frac{1}{c^2(\boldsymbol{x})} = \frac{1}{c_0^2}\big(1 + \sigma_r \mathbf{1}_{\Omega_r}(\boldsymbol{x} - \boldsymbol{z}_r)\big), \tag{2.1}$$

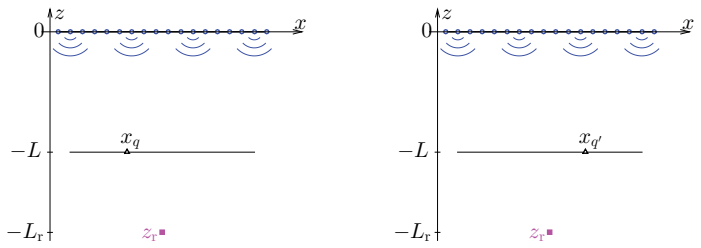

Figure 3. *Passive synthetic aperture imaging configuration. Two positions $\boldsymbol{x}_q$ and $\boldsymbol{x}_{q'}$ of the receiver in the plane $z = -L$ are plotted. The noise sources are distributed at the surface $z = 0$. $\boldsymbol{z}_r$ is a reflector at $z = -L_r$.*

where Ω_r is a small domain with volume l_r^3 and σ_r is the reflectivity of the reflector. This is a typical situation in PSA radar imaging [11]. The moving receiver antenna takes the successive positions $\boldsymbol{x}_q$ at times T_q, $q = 1, \ldots, N_q$, and records the wave field during the time interval $[T_q, T_q + T]$. We consider the stop-go approximation; that is to say, the receiver antenna is assumed to be stationary at $\boldsymbol{x}_q$ during the recording time window $[T_q, T_q + T]$.

The data set then consists of the signals recorded by the receiver at $\boldsymbol{x}_q$:

$$\big\{u(t, \boldsymbol{x}_q),\, t \in [T_q, T_q + T]\,, q = 1, \ldots, N_q\big\}, \tag{2.2}$$

where $u(t, \boldsymbol{x})$ is the wave field generated by the noise sources and is solution to

$$\frac{1}{c^2(\boldsymbol{x})}\frac{\partial^2 u}{\partial t^2} - \Delta_{\boldsymbol{x}} u = n^\varepsilon(t, \boldsymbol{x}_\perp)\delta(z), \tag{2.3}$$

with the speed of propagation of the form (2.1). The source term $n^\varepsilon(t, \boldsymbol{x}_\perp)$ models the noise sources, and we model it as a realization of a random process with mean zero and covariance of the form

$$\big\langle n^\varepsilon(t, \boldsymbol{x}_\perp) n^\varepsilon(t', \boldsymbol{x}'_\perp)\big\rangle = \psi_s(\boldsymbol{x}_\perp)\delta(\boldsymbol{x}_\perp - \boldsymbol{x}'_\perp)F^\varepsilon(t - t'). \tag{2.4}$$

Here $\langle\cdot\rangle$ stands for the statistical average with respect to the distribution of the noise sources. For simplicity we consider that the process n^ε has Gaussian statistics. The time distribution of the noise sources is characterized by the correlation function $F^\varepsilon(t - t')$, which is a function of $t - t'$ only, which means that the process is stationary. The function F^ε is normalized so that $F^\varepsilon(0) = 1$. It depends on a scale parameter ε, which we will describe in the next section devoted to the high-frequency analysis. The Fourier transform $\hat{F}^\varepsilon(\omega)$ of the time correlation function $F^\varepsilon(t)$ is a nonnegative, even, real-valued function proportional to the power spectral density of the noise sources:

$$\hat{F}^\varepsilon(\omega) = \int_{\mathbb{R}} F^\varepsilon(t) e^{i\omega t} \mathrm{d}t. \tag{2.5}$$

The spatial distribution of the noise sources is characterized by the autocovariance function $\psi_s(\boldsymbol{x}_\perp)\delta(\boldsymbol{x}_\perp - \boldsymbol{x}'_\perp)$, which means that the random process $n^\varepsilon(t, \boldsymbol{x}_\perp)$ is delta-correlated in space

and that the source density function $\psi_{\rm s}(\boldsymbol{x}_\perp)$ characterizes the spatial support of the noise sources.

Note that we have assumed that the sources lie on a surface. We could also have considered the case of a volume source distribution, as is done in [13]. This would not qualitatively affect the results. The reason why we have chosen the surface is that it corresponds to some physically relevant situations, in underwater acoustics for instance (see below), and we can define the diameter of the source region in a straightforward manner.

The empirical autocorrelation functions from the data set (2.2) have the form

$$\mathcal{C}_T(\tau,\boldsymbol{x}_q)=\frac{1}{T-\tau}\int_{T_q}^{T_q+T-\tau} u(t,\boldsymbol{x}_q)u(t+\tau,\boldsymbol{x}_q)\mathrm{d}t \tag{2.6}$$

for $\tau\geq 0$ and $q=1,\ldots,N_{\rm q}$. Note that the integral in t is taken over the largest interval such that t and $t+\tau$ are both in the recording time window $[T_q,T_q+T]$.

From the general theory of correlation-based imaging [13, 14], we expect that the autocorrelation function $\mathcal{C}_T(\tau,\boldsymbol{x}_q)$ is related to the Green's function between $\boldsymbol{x}_q$ and $\boldsymbol{x}_q$, that is, the signal that would be acquired at $\boldsymbol{x}_q$ when there is a point source at $\boldsymbol{x}_q$ emitting a short pulse. In fact we will show in Proposition 3.2 that the autocorrelation function $\tau\to\mathcal{C}_T(\tau,\boldsymbol{x}_q)$ has a peak at lag time equal to twice the travel time from $\boldsymbol{x}_q$ to $\boldsymbol{z}_{\rm r}$. As a consequence, a natural imaging function is the PSA migration function

$$\mathcal{I}_{\rm psa}(\boldsymbol{z}^S)=\sum_{q=1}^{N_{\rm q}}\mathcal{C}_T\big(2\mathcal{T}(\boldsymbol{x}_q,\boldsymbol{z}^S),\boldsymbol{x}_q\big), \tag{2.7}$$

where $\mathcal{T}(\boldsymbol{x},\boldsymbol{z})$ is the travel time:

$$\mathcal{T}(\boldsymbol{x},\boldsymbol{z})=\frac{|\boldsymbol{x}-\boldsymbol{z}|}{c_0}. \tag{2.8}$$

We show in the following that the PSA imaging function (2.7) gives a good image of the reflector.

Remark. In this paper, we do not address sampling issues and consider that the sampling rate at which the signals are recorded in time is high enough (say, larger than the Nyquist frequency), so that we can assume that the continuous signals are available. We also assume that the noise sources and the synthetic receiver array (determined by the successive positions of the receiver antenna) are dense, so that we can replace certain discrete sums by continuous integrals. Sampling is, however, a critical issue that needs to be addressed, and this will be done in a further work. We also assume the stop-go approximation, which means that the moving antenna goes from one position to the next one and can be considered as stationary during the recording process at each position. This means that we can neglect Doppler effects. If the moving antenna is a vehicle or a low-speed platform, this hypothesis is reasonable (as in [7], for instance), but Doppler effects should be taken into account when the moving antenna is a high-speed platform [27].

For completeness we briefly describe two experimental environments that would be compatible with these assumptions.

In passive underwater acoustics, at frequencies of more than several hundred Hz and less than 20 kHz, the breaking waves are commonly the predominant source of ambient noise [17, 23, 25]. The surface noise generated by breaking waves can be approximated as a sheet of noise sources just below the surface [17]. Experiments have demonstrated that coherent wave fronts can be recovered from the cross correlations of the ocean's ambient noise signals [23]. Based on this idea, a method called passive fathometry has been developed that exploits the correlation properties of the ocean's ambient noise to measure water depth [25]. In these experiments the central frequency and the bandwidth are on the order of a few hundred Hz, the typical distance between the receiver antenna and the target is on the order of 100 meters, the receiver antenna is drifting at very low velocity, and the recording time window is on the order of minutes. There is no sampling issue in this setting.

In PSA radar configurations using illumination from satellites and an airborne passive platform, the typical numbers are the following: the carrier frequency is on the order of 10 GHz, the bandwidth is on the order of a few tens or a few hundreds of MHz, and the length of the flight path over which the acquisition is carried out (whose duration is on the order of a few seconds) is on the order of a few hundred meters. The height of the airborne platform and the distance from the platform to the target are on the order of 10 km [20, 21]. As noted in [20], continuous or quasi-continuous data acquisition capability of the receiver antenna is a critical experimental ingredient.

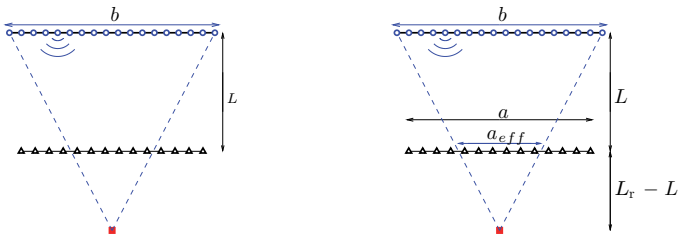

Figure 4. *Left: Definition of the illumination cone, which contains all rays going from the reflector to the noise source region with diameter b. Right: The intersection of the illumination cone with the plane of the receiver antenna determines the effective synthetic receiver array with diameter* a_{eff}*. The successive positions of the receiver antenna define the physical synthetic receiver array with diameter a.*

2.2. Summary of the main results. An important aspect of the problem is the characterization of the illumination diversity. The rays (which are straight lines in a homogeneous medium) that go from points in the noise source region in the plane $z = 0$ to the reflector determine an illumination cone for the reflector (see Figure 4(left)). Roughly speaking, only the receiver positions that are within this illumination cone give useful information about the reflector. This corresponds to an effective synthetic receiver array diameter a_{eff} (defined as the intersection of the illumination cone with the plane of the receiver antenna) given by (see Figure 4(right))

$$a_{\text{eff}} = b\frac{L_{\text{r}} - L}{L_{\text{r}}}, \tag{2.9}$$

where b is the diameter of the noise source region. As a result, the cross-range resolution of the PSA imaging function (2.7) is given by the effective Rayleigh resolution formula $\lambda_0(L_{\rm r}-L)/\bar{a}_{\rm eff}$, where λ_0 is the central wavelength of the noise sources, $\bar{a}_{\rm eff} = \min(a_{\rm eff}, a)$, and a is the physical diameter of the synthetic receiver array determined by the successive positions of the receiver antenna. The range resolution is given by c_0/B, where B is the noise source bandwidth. The detailed analysis is carried out in the high-frequency regime in the next section.

We also show that the resolution of the PSA imaging function (2.7) is equivalent to that of the matched filter imaging function used in active synthetic aperture imaging (4.4) when the moving antenna is both a source and a receiver, provided that the illumination in the passive configuration is diversified so that $a_{\rm eff} > a$.

3. High-frequency analysis.

We assume that the decoherence time of the noise sources (which is the inverse of the bandwidth of the power spectral density) is much smaller than the typical travel time between the antenna and the reflector. If we denote with ε the (small) ratio of these two time scales, we can then write the time correlation function F^ε in the form

$$F^\varepsilon(t-t') = F\left(\frac{t-t'}{\varepsilon}\right), \tag{3.1}$$

where t and t' are scaled relative to typical travel times.

3.1. The autocorrelation function in terms of the Green's function.

The solution of the wave equation with source $n^\varepsilon(t,\boldsymbol{x}_\perp)\delta(z)$ can be expressed as the convolution of the Green's function and the source term:

$$u(t,\boldsymbol{x}) = \int_{\mathbb{R}}\int_{\mathbb{R}^2} G\big(t-s,\boldsymbol{x},(\boldsymbol{y}_\perp,0)\big) n^\varepsilon(s,\boldsymbol{y}_\perp)\mathrm{d}\boldsymbol{y}_\perp\,\mathrm{d}s. \tag{3.2}$$

Here the time-dependent Green's function $G(t,\boldsymbol{x},\boldsymbol{y})$ is the fundamental solution of the wave equation

$$\frac{1}{c^2(\boldsymbol{x})}\frac{\partial^2 G}{\partial t^2} - \Delta_{\boldsymbol{x}} G = \delta(t)\delta(\boldsymbol{x}-\boldsymbol{y}), \tag{3.3}$$

with the speed of propagation of the form (2.1) and with the initial conditions

$$G(t,\boldsymbol{x},\boldsymbol{y}) = 0 \qquad \forall t<0. \tag{3.4}$$

We can proceed as in [13] to show the following proposition. For completeness we give the proof in Appendix A.

Proposition 3.1.

1. *The expectation of the empirical autocorrelation function* (2.7) *is equal to the statistical autocorrelation function:*

$$\mathcal{C}(\tau,\boldsymbol{x}_q) = \frac{1}{2\pi}\int_{\mathbb{R}} \mathrm{d}\omega \hat{F}^\varepsilon(\omega) \int_{\mathbb{R}^2} \mathrm{d}\boldsymbol{y}_\perp \psi_{\rm s}(\boldsymbol{y}_\perp)|\hat{G}\big(\omega,\boldsymbol{x}_q,(\boldsymbol{y}_\perp,0)\big)|^2 \exp\big(-i\omega\tau\big), \tag{3.5}$$

where $\hat{G}(\omega,\boldsymbol{x},\boldsymbol{y})$ *is the time-harmonic Green's function,*

$$\frac{\omega^2}{c^2(\boldsymbol{x})}\hat{G}(\omega,\boldsymbol{x},\boldsymbol{y}) + \Delta_{\boldsymbol{x}}\hat{G}(\omega,\boldsymbol{x},\boldsymbol{y}) = -\delta(\boldsymbol{x}-\boldsymbol{y}), \tag{3.6}$$

the speed of propagation is (2.1)*, and the power spectral density* $\hat{F}^\varepsilon$ *is of the form*

$$\hat{F}^\varepsilon(\omega) = \varepsilon \hat{F}(\varepsilon\omega)\,. \tag{3.7}$$

2. *The empirical autocorrelation* $\mathcal{C}_T$ *is a self-averaging quantity,*

$$\mathcal{C}_T(\tau, \boldsymbol{x}_q) \overset{T\to\infty}{\longrightarrow} \mathcal{C}(\tau, \boldsymbol{x}_q), \tag{3.8}$$

in probability with respect to the distribution of the noise sources.

The second point means that, provided the recording time T is long enough, the empirical autocorrelation function (2.7) is equal to the statistical autocorrelation function (3.5). The analysis in the next section addresses the behavior of the statistical autocorrelation function.

Remark. We have made two assumptions about the recording time T: it should be small enough so that the stop-go approximation is valid, and it should be large enough so that the statistical stability of the empirical autocorrelation function is achieved. The detailed proof in Appendix A shows that self-averaging is actually achieved as soon as $(T-\tau)/\varepsilon \gg 1$. As we will see below, the piece of the autocorrelation function that is of interest for reflector imaging is for time lags around twice the travel time from the receiver antenna to the reflector. Therefore, this shows that the recording time T should be slightly larger than twice the typical travel time from the receiver to the search region to ensure that the contribution of interest is captured in a statistically stable way. This constraint is compatible with the stop-go approximation. In fact, it is of the same order as the constraint for the stop-go approximation in the classical, active synthetic aperture configuration, which also requires that the motion of the receiver antenna can be neglected while the emitted wave carries a round trip from the antenna to the reflector (see section 4).

3.2. High-frequency analysis of the autocorrelation function. From this point on in this section we assume that the typical travel time is much larger than the decoherence time of the noise sources, so that it is relevant to study the high-frequency regime $\varepsilon \to 0$. We carry out the analysis when the background medium is homogeneous and there is a point reflector at $\boldsymbol{z}_\mathrm{r}$ as modeled by (2.1). Since we assume that the reflector is weak, we use the Born approximation for the Green's function. If, moreover, the reflector has small support (smaller than the typical wavelength), then we get the point-like approximation:

$$\hat{G}(\omega, \boldsymbol{x}, \boldsymbol{y}) = \hat{G}_0(\omega, \boldsymbol{x}, \boldsymbol{y}) + \frac{\omega^2}{c_0^2}\sigma_\mathrm{r} l_\mathrm{r}^3 \hat{G}_0(\omega, \boldsymbol{x}, \boldsymbol{z}_\mathrm{r})\hat{G}_0(\omega, \boldsymbol{z}_\mathrm{r}, \boldsymbol{y})\,. \tag{3.9}$$

Here $\hat{G}_0$ is the Green's function of the background medium, that is, in the absence of reflector:

$$\frac{\omega^2}{c_0^2}\hat{G}_0(\omega, \boldsymbol{x}, \boldsymbol{y}) + \Delta_{\boldsymbol{x}}\hat{G}_0(\omega, \boldsymbol{x}, \boldsymbol{y}) = -\delta(\boldsymbol{x} - \boldsymbol{y}). \tag{3.10}$$

The autocorrelation in the presence of the reflector can be written as

$$\mathcal{C}(\tau, \boldsymbol{x}_q) = \mathcal{C}_0(\tau, \boldsymbol{x}_q) + \Delta\mathcal{C}(\tau, \boldsymbol{x}_q), \tag{3.11}$$

where $\mathcal{C}_0$ is the background autocorrelation in the absence of the reflector (i.e., (3.5) with the background Green's function $\hat{G}_0$ given by (3.10)) and $\Delta\mathcal{C}$ is the differential autocorrelation.

The background autocorrelation function $\mathcal{C}_0$, as a function of the lag time, is supported in a short interval of duration on the order of ε:

$$\mathcal{C}_0(\tau,\boldsymbol{x}_q)=\frac{1}{16\pi^2}\left[\int_{\mathbb{R}^2}\mathrm{d}\boldsymbol{y}_\perp\frac{\psi_{\mathrm{s}}(\boldsymbol{y}_\perp)}{|\boldsymbol{x}_q-(\boldsymbol{y}_\perp,0)|^2}\right]F\Big(\frac{\tau}{\varepsilon}\Big). \tag{3.12}$$

In order to study the differential autocorrelation $\Delta\mathcal{C}$ we collect the terms with the same power in $\sigma_{\mathrm{r}}l_{\mathrm{r}}^3$. We retain only the terms of order $O(\sigma_{\mathrm{r}}l_{\mathrm{r}}^3)$, consistent with the Born approximation:

$$\Delta\mathcal{C}(\tau,\boldsymbol{x}_q)=\Delta\mathcal{C}_{\mathrm{I}}(\tau,\boldsymbol{x}_q)+\Delta\mathcal{C}_{\mathrm{II}}(\tau,\boldsymbol{x}_q), \tag{3.13}$$

$$\begin{aligned}\Delta\mathcal{C}_{\mathrm{I}}(\tau,\boldsymbol{x}_q)=&\frac{\sigma_{\mathrm{r}}l_{\mathrm{r}}^3}{2\pi c_0^2\varepsilon^2}\int_{\mathbb{R}^2}\mathrm{d}\boldsymbol{y}_\perp\int_{\mathbb{R}}\mathrm{d}\omega\psi_{\mathrm{s}}(\boldsymbol{y}_\perp)\omega^2\hat{F}(\omega)\overline{\hat{G}_0}\Big(\frac{\omega}{\varepsilon},\boldsymbol{x}_q,\boldsymbol{z}_{\mathrm{r}}\Big)\\&\times\overline{\hat{G}_0}\left(\frac{\omega}{\varepsilon},\boldsymbol{z}_{\mathrm{r}},(\boldsymbol{y}_\perp,0)\right)\hat{G}_0\left(\frac{\omega}{\varepsilon},\boldsymbol{x}_q,(\boldsymbol{y}_\perp,0)\right)\exp\left(-i\frac{\omega\tau}{\varepsilon}\right),\end{aligned} \tag{3.14}$$

$$\begin{aligned}\Delta\mathcal{C}_{\mathrm{II}}(\tau,\boldsymbol{x}_q)=&\frac{\sigma_{\mathrm{r}}l_{\mathrm{r}}^3}{2\pi c_0^2\varepsilon^2}\int_{\mathbb{R}^2}\mathrm{d}\boldsymbol{y}_\perp\int_{\mathbb{R}}\mathrm{d}\omega\psi_{\mathrm{s}}(\boldsymbol{y}_\perp)\omega^2\hat{F}(\omega)\overline{\hat{G}_0}\Big(\frac{\omega}{\varepsilon},\boldsymbol{x}_q,(\boldsymbol{y}_\perp,0)\Big)\\&\times\hat{G}_0\Big(\frac{\omega}{\varepsilon},\boldsymbol{x}_q,\boldsymbol{z}_{\mathrm{r}}\Big)\hat{G}_0\Big(\frac{\omega}{\varepsilon},\boldsymbol{z}_{\mathrm{r}},(\boldsymbol{y}_\perp,0)\Big)\exp\Big(-i\frac{\omega\tau}{\varepsilon}\Big),\end{aligned} \tag{3.15}$$

where we have used the form (3.7) of the power spectral density. The autocorrelation function contains information about the reflector location in the form of peaks at lag times equal to plus or minus twice the travel time from the receiver to the reflector, as explained in the following proposition proved in Appendix B.

Proposition 3.2. *In the asymptotic regime $\varepsilon\to 0$, the differential autocorrelation function has two peaks centered at plus or minus twice the travel time $\mathcal{T}(\boldsymbol{x}_q,\boldsymbol{z}_{\mathrm{r}})$:*

$$\Delta\mathcal{C}(\tau,\boldsymbol{x}_q)\approx\frac{\sigma_{\mathrm{r}}l_{\mathrm{r}}^3}{32\pi^2c_0}\frac{\mathcal{K}(\boldsymbol{x}_q,\boldsymbol{z}_{\mathrm{r}})}{|\boldsymbol{z}_{\mathrm{r}}-\boldsymbol{x}_q|^2}\left[\partial_\tau F\left(\frac{\tau-2\mathcal{T}(\boldsymbol{x}_q,\boldsymbol{z}_{\mathrm{r}})}{\varepsilon}\right)-\partial_\tau F\left(\frac{\tau+2\mathcal{T}(\boldsymbol{x}_q,\boldsymbol{z}_{\mathrm{r}})}{\varepsilon}\right)\right]. \tag{3.16}$$

Here we have defined

$$\mathcal{K}(\boldsymbol{x}_q,\boldsymbol{z}_{\mathrm{r}})=\psi_{\mathrm{s}}\big(\boldsymbol{Y}_\perp(\boldsymbol{x}_{q_\perp})\big)\frac{|\boldsymbol{x}_q-\boldsymbol{z}_{\mathrm{r}}|}{L_{\mathrm{r}}-L}, \tag{3.17}$$

$$\boldsymbol{Y}_\perp(\boldsymbol{x}_{q_\perp})=\frac{\boldsymbol{x}_{q_\perp}L_{\mathrm{r}}-\boldsymbol{z}_{\mathrm{r}_\perp}L}{L_{\mathrm{r}}-L}. \tag{3.18}$$

Note that $(\boldsymbol{Y}_\perp(\boldsymbol{x}_{q_\perp}),0)$ is the intersection of the line going through $\boldsymbol{x}_q=(\boldsymbol{x}_{q_\perp},-L)$ and $\boldsymbol{z}_{\mathrm{r}}=(\boldsymbol{z}_{\mathrm{r}_\perp},-L_{\mathrm{r}})$ with the plane $z=0$. Since the support of the source density function ψ_{s} is the spatial support of the noise source distribution, this implies that there are peaks in the autocorrelation function associated to the reflector if and only if there are rays going through the noise source region, the receiver position, and the reflector location.

3.3. High-frequency analysis of the PSA migration function. We consider and study the imaging function (2.7) in the regime $\varepsilon\to 0$. By Proposition 3.1 and (3.11), it is given by

$$\mathcal{I}_{\mathrm{psa}}(\boldsymbol{z}^S)=\sum_{q=1}^{N_{\mathrm{q}}}\mathcal{C}_0\big(2\mathcal{T}(\boldsymbol{x}_q,\boldsymbol{z}^S),\boldsymbol{x}_q\big)+\sum_{q=1}^{N_{\mathrm{q}}}\Delta\mathcal{C}\big(2\mathcal{T}(\boldsymbol{x}_q,\boldsymbol{z}^S),\boldsymbol{x}_q\big).$$

Note first that the background autocorrelation $\tau \to \mathcal{C}_0(\tau, \boldsymbol{x}_q)$ does not give any contribution to the imaging function because its support is within the interval centered at 0 and of width of order ε, as shown by (3.12), while the imaging function evaluates the autocorrelation at time lag $2\mathcal{T}(\boldsymbol{x}_q, \boldsymbol{z}^S)$. Second, assuming that the successive positions of the moving receiver antenna are close enough, we can replace the discrete sum over q by a continuous integral:

$$\mathcal{I}_{\mathrm{psa}}(\boldsymbol{z}^S) = \int_{\mathbb{R}^2} \mathrm{d}\boldsymbol{x}_\perp \, \psi_{\mathrm{q}}(\boldsymbol{x}_\perp) \Delta\mathcal{C}\big(2\mathcal{T}((\boldsymbol{x}_\perp, -L), \boldsymbol{z}^S), (\boldsymbol{x}_\perp, -L)\big), \tag{3.19}$$

where ψ_{q} is the synthetic receiver array density function, such that

$$\int_A \psi_{\mathrm{q}}(\boldsymbol{x}_\perp)\mathrm{d}\boldsymbol{x}_\perp = \mathrm{Card}\,\{q = 1, \dots, N_{\mathrm{q}},\, \boldsymbol{x}_q \in A\}\,, \qquad \int_{\mathbb{R}^2} \psi_{\mathrm{q}}(\boldsymbol{x}_\perp)\mathrm{d}\boldsymbol{x}_\perp = N_{\mathrm{q}}. \tag{3.20}$$

We then get the following proposition, proved in Appendix C.

Proposition 3.3. *In the asymptotic regime $\varepsilon \to 0$, we have*

$$\begin{aligned}\mathcal{I}_{\mathrm{psa}}(\boldsymbol{z}^S) = {} & \frac{\sigma_{\mathrm{r}} l_{\mathrm{r}}^3}{64\pi^3 c_0 \varepsilon} \int_{\mathbb{R}^2} \mathrm{d}\boldsymbol{x}_\perp \frac{\psi_{\mathrm{q}}(\boldsymbol{x}_\perp)\psi_{\mathrm{s}}(\boldsymbol{Y}_\perp(\boldsymbol{x}_\perp))}{(L_{\mathrm{r}} - L)|\boldsymbol{z}_{\mathrm{r}} - (\boldsymbol{x}_\perp, -L)|} \\ & \times \int_{\mathbb{R}} \mathrm{d}\omega \, i\omega \hat{F}(\omega) \exp\left[-2i\frac{\omega}{c_0}\frac{\boldsymbol{z}^S - \boldsymbol{z}_{\mathrm{r}}}{\varepsilon} \cdot \frac{(\boldsymbol{x}_\perp, -L) - \boldsymbol{z}_{\mathrm{r}}}{|(\boldsymbol{x}_\perp, -L) - \boldsymbol{z}_{\mathrm{r}}|}\right].\end{aligned} \tag{3.21}$$

In the next corollary we make a few assumptions that will allow us to get an explicit expression of the point spread function of the imaging function. These assumptions are that the noise sources are supported on a square with sidelength b at the surface $z = 0$, that the synthetic receiver array is square with sidelength a, that the reflector is just below them at a distance larger than the synthetic receiver array diameter, and that the width B of the power spectral density $\hat{F}$ is smaller than its central frequency ω_0.

Corollary 3.4. *Let us assume that $\boldsymbol{z}_{\mathrm{r}} = (0, 0, -L_{\mathrm{r}})$, $\psi_{\mathrm{s}}(\boldsymbol{x}_\perp) = \frac{1}{b^2}\mathbf{1}_{[-b/2,b/2]^2}(\boldsymbol{x}_\perp)$, $\psi_{\mathrm{q}}(\boldsymbol{x}_\perp) = \frac{N_{\mathrm{q}}}{a^2}\mathbf{1}_{[-a/2,a/2]^2}(\boldsymbol{x}_\perp)$, $L_{\mathrm{r}} - L \gg a$, and $\omega_0 \gg B$. We parameterize the search point as*

$$\boldsymbol{z}^S = \boldsymbol{z}_{\mathrm{r}} + \varepsilon(\xi_1, \xi_2, \eta).$$

Then

$$\begin{aligned}\mathcal{I}_{\mathrm{psa}}(\boldsymbol{z}^S) = {} & -\frac{\sigma_{\mathrm{r}} l_{\mathrm{r}}^3 N_{\mathrm{q}} \bar{a}_{\mathrm{eff}}^2}{32\pi^2 c_0 a^2 b^2 (L_{\mathrm{r}} - L)^2 \varepsilon} \partial_\tau F\Big(\frac{2\eta}{c_0}\Big) \\ & \times \mathrm{sinc}\left(\frac{\omega_0 \bar{a}_{\mathrm{eff}}}{c_0(L_{\mathrm{r}} - L)}\xi_1\right) \mathrm{sinc}\left(\frac{\omega_0 \bar{a}_{\mathrm{eff}}}{c_0(L_{\mathrm{r}} - L)}\xi_2\right),\end{aligned} \tag{3.22}$$

where $\bar{a}_{\mathrm{eff}} = \min(a_{\mathrm{eff}}, a)$ and a_{eff} is defined by (2.9).

The expressions of $\bar{a}_{\mathrm{eff}}$ and $a_{\mathrm{eff}} = b(L_{\mathrm{r}} - L)/L_{\mathrm{r}}$ come from the fact that $\boldsymbol{Y}_\perp(\boldsymbol{x}_\perp) = \frac{L_{\mathrm{r}}}{L_{\mathrm{r}} - L}\boldsymbol{x}_\perp$ and therefore

$$\psi_{\mathrm{q}}(\boldsymbol{x}_\perp)\psi_{\mathrm{s}}(\boldsymbol{Y}_\perp(\boldsymbol{x}_\perp)) = \frac{1}{b^2}\frac{N_{\mathrm{q}}}{a^2}\mathbf{1}_{[-\bar{a}_{\mathrm{eff}}/2,\bar{a}_{\mathrm{eff}}/2]^2}(\boldsymbol{x}_\perp).$$

The effective synthetic receiver array diameter a_{eff} has a simple geometric interpretation as the diameter of the intersection of the illumination cone with the plane of the synthetic receiver array (see Figure 4).

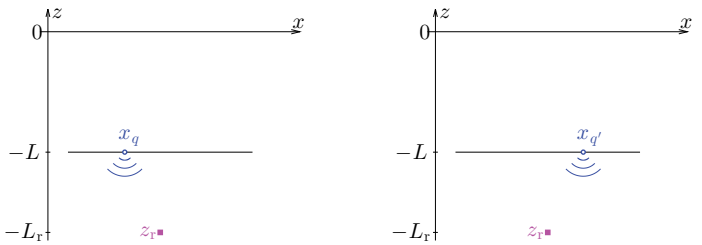

Figure 5. *ASA imaging configuration. Two positions $\boldsymbol{x}_q$ and $\boldsymbol{x}_{q'}$ of the source-receiver antenna in the plane $z = -L$ are plotted. $\boldsymbol{z}_r$ is a reflector at $z = -L_r$.*

This corollary shows that the point spread function of the PSA migration function in the transverse variables has the form of a sinc with a radius given by the "effective" Rayleigh resolution formula $\lambda_0(L_r - L)/(2\bar{a}_{\rm eff})$, where $\lambda_0 = 2\pi c_0/\omega_0$ is the central wavelength of the noise sources, while the resolution in the longitudinal variable is determined by the bandwidth of the noise sources. This shows that diversity of illumination, that is, a large illumination cone, is necessary to get good cross-range resolution.

As soon as the illumination cone is so large that $a_{\rm eff} > a$, then the resolution of the image obtained by PSA is the standard resolution formula for an active array of diameter a. More exactly, we show in the next section that the PSA migration function (2.7) is equivalent to the matched filter imaging function used in active synthetic aperture imaging.

Similar results can be obtained in a two-dimensional configuration. In fact, the numerical simulations presented in section 6 are carried out in a two-dimensional setup.

4. Comparison with classical synthetic aperture imaging. In this section we address a classical imaging situation called synthetic aperture imaging. In order to distinguish it from the previous situation we will call it active synthetic aperture (ASA) imaging, because, in this situation, a single source-receiver antenna is moving and recording the signals generated by itself (see Figure 5). The successive positions of the source-receiver are $(\boldsymbol{x}_q)_{q=1}^{N_q}$, which lie in the plane $z = -L$. For each position $\boldsymbol{x}_q$, the source emits the short pulse $f^\varepsilon(t - T_q)$ of the form

$$f^\varepsilon(t) = f\left(\frac{t}{\varepsilon}\right), \qquad \hat{f}(\omega) = \sqrt{\hat{F}(\omega)}, \tag{4.1}$$

and the signal is recorded by the coincident receiver. The data set is

$$\left\{v_q(t, \boldsymbol{x}_q),\, t \in [T_q + \Delta T, T_q + T],\, q = 1, \ldots, N_q\right\}, \tag{4.2}$$

where $v_q(t, \boldsymbol{x})$ is the solution of

$$\frac{1}{c^2(\boldsymbol{x})}\frac{\partial^2 v_q}{\partial t^2} - \Delta_{\boldsymbol{x}} v_q = f^\varepsilon(t - T_q)\delta(\boldsymbol{x} - \boldsymbol{x}_q);$$

the time ΔT is larger than the pulse width and smaller than twice the travel time from the synthetic array to the reflector; and the time T is larger than twice the travel time from the

synthetic array to the reflector. As a result, $t \to v_q(t, \boldsymbol{x}_q)$ contains only the backscattered signal and not the direct emission. We may interpret the data set (4.2) as the diagonal part of the array response matrix of an active array at $(\boldsymbol{x}_q)_{q=1}^{N_\mathrm{q}}$.

If we assume that there is a point reflector at $\boldsymbol{z}_\mathrm{r}$ in the plane $z = -L_\mathrm{r}$ with reflectivity σ_r and volume l_r^3, as in the previous section, then the Fourier transform $\hat{v}_q(\omega, \boldsymbol{x}_q)$ has the form

$$\hat{v}_q(\omega, \boldsymbol{x}_q) = \frac{\sigma_\mathrm{r} l_\mathrm{r}^3 \omega^2}{c_0^2} \hat{G}_0(\omega, \boldsymbol{x}_q, \boldsymbol{z}_\mathrm{r})^2 \hat{f}^\varepsilon(\omega) e^{i\omega T_q}.$$

The Kirchhoff migration function for this synthetic aperture configuration is therefore

$$\mathcal{I}_{\mathrm{KMasa}}(\boldsymbol{z}^S) = \sum_{q=1}^{N_\mathrm{q}} v_q\big(T_q + 2\mathcal{T}(\boldsymbol{x}_q, \boldsymbol{z}^S), \boldsymbol{x}_q\big), \tag{4.3}$$

with the travel time $\mathcal{T}$ given by (2.8). However, the most standard imaging method is the matched filter imaging function, or ASA function [7]:

$$\mathcal{I}_{\mathrm{asa}}(\boldsymbol{z}^S) = \frac{1}{2\pi} \sum_{q=1}^{N_\mathrm{q}} \int_{\mathbb{R}} \overline{\hat{f}^\varepsilon(\omega)} \hat{v}_q(\omega, \boldsymbol{x}_q) \exp\big(-i\omega(T_q + 2\mathcal{T}(\boldsymbol{x}_q, \boldsymbol{z}^S))\big) \mathrm{d}\omega. \tag{4.4}$$

This imaging method is preferred to Kirchhoff migration because it is the optimal linear filter in the sense of signal-to-noise ratio with respect to measurement noise and can be implemented with low requirements on the sampling rate [8]. In our framework, we do not take into account any additive measurement noise, and we assume that we can record continuous signals, so there is actually no difference in the two imaging methods. Now the following results are true for the Kirchhoff migration function (4.3), provided that F is replaced by f.

We carry out the high-frequency analysis of the imaging function (4.4) in the case where the successive positions $(\boldsymbol{x}_q)_{q=1}^{N_\mathrm{q}}$ in the plane $z = -L$ form a dense synthetic array with the array density function ψ_q as in (3.20).

Proposition 4.1. *In the asymptotic regime $\varepsilon \to 0$, we have*

$$\begin{aligned} \mathcal{I}_{\mathrm{asa}}(\boldsymbol{z}^S) = {} & \frac{\sigma_\mathrm{r} l_\mathrm{r}^3}{32\pi^3 c_0^2 \varepsilon} \int_{\mathbb{R}^2} \mathrm{d}\boldsymbol{x}_\perp \frac{\psi_\mathrm{q}(\boldsymbol{x}_\perp)}{|\boldsymbol{z}_\mathrm{r} - (\boldsymbol{x}_\perp, -L)|^2} \\ & \times \int_{\mathbb{R}} \mathrm{d}\omega\, \omega^2 \hat{F}(\omega) \exp\left[-2i \frac{\omega}{c_0} \frac{\boldsymbol{z}^S - \boldsymbol{z}_\mathrm{r}}{\varepsilon} \cdot \frac{(\boldsymbol{x}_\perp, -L) - \boldsymbol{z}_\mathrm{r}}{|(\boldsymbol{x}_\perp, -L) - \boldsymbol{z}_\mathrm{r}|}\right]. \end{aligned} \tag{4.5}$$

In the next corollary we make a few assumptions (as in Corollary 3.4) that allow us to get an explicit expression of the point spread function of the imaging function.

Corollary 4.2. *Let us assume that $\boldsymbol{z}_\mathrm{r} = (0, 0, -L_\mathrm{r})$, $\psi_\mathrm{q}(\boldsymbol{x}_\perp) = \frac{N_\mathrm{q}}{a^2} \mathbf{1}_{[-a/2, a/2]^2}(\boldsymbol{x}_\perp)$, $L_\mathrm{r} - L \gg a$, and $\omega_0 \gg B$. We parameterize the search point as*

$$\boldsymbol{z}^S = \boldsymbol{z}_\mathrm{r} + \varepsilon(\xi_1, \xi_2, \eta).$$

Then

$$\begin{aligned} \mathcal{I}_{\mathrm{asa}}(\boldsymbol{z}^S) = {} & -\frac{\sigma_\mathrm{r} l_\mathrm{r}^3 N_\mathrm{q}}{16\pi^2 c_0^2 (L_\mathrm{r} - L)^2 \varepsilon} \partial_\tau^2 F\left(\frac{2\eta}{c_0}\right) \\ & \times \mathrm{sinc}\left(\frac{\omega_0 a}{c_0(L_\mathrm{r} - L)} \xi_1\right) \mathrm{sinc}\left(\frac{\omega_0 a}{c_0(L_\mathrm{r} - L)} \xi_2\right). \end{aligned} \tag{4.6}$$

By comparing Propositions 3.3 and 4.1, or Corollaries 3.4 and 4.2, we can see that the resolution of PSA imaging function (2.7) is equivalent to that of ASA imaging function (4.4), provided that the illumination in the passive configuration is diversified so that $a_{\rm eff} > a$.

5. Discussion.

5.1. Time-reversal interpretation of PSA imaging. We wish to emphasize that the reason why PSA imaging works so well is because, by wave field reciprocity, the autocorrelation function $\mathcal{C}(\tau, \boldsymbol{x}_q)$ can be given a time-reversal interpretation, a well-known observation [9, 10, 18] that we discuss briefly here. Indeed, if we use the reciprocity property of the Green's function, then the autocorrelation function (3.5),

$$\mathcal{C}(\tau, \boldsymbol{x}_q) = \int_{\mathbb{R}^2} \mathrm{d}\boldsymbol{y}_\perp \psi_{\rm s}(\boldsymbol{y}_\perp) \int_{\mathbb{R}} \hat{F}^\varepsilon(\omega) \big|\hat{G}(\omega, \boldsymbol{x}_q, (\boldsymbol{y}_\perp, 0))\big|^2 \exp(-i\omega\tau)\mathrm{d}\omega,$$

can be written as

$$\mathcal{C}(\tau, \boldsymbol{x}_q) = \int_{\mathbb{R}^2} \mathrm{d}\boldsymbol{y}_\perp \int_{\mathbb{R}} \hat{G}(\omega, \boldsymbol{x}_q, (\boldsymbol{y}_\perp, 0)) \psi_{\rm s}(\boldsymbol{y}_\perp) \overline{\hat{F}^\varepsilon(\omega) \hat{G}(\omega, (\boldsymbol{y}_\perp, 0), \boldsymbol{x}_q)} \exp(-i\omega\tau)\mathrm{d}\omega.$$

This is the field observed at $\boldsymbol{x}_q$ during a time-reversal experiment in which (1) an original source at $\boldsymbol{x}_q$ emits a short pulse of the form $F^\varepsilon(t)$ and (2) a time-reversal array (whose spatial support is on the surface $z = 0$ with the density function $\psi_{\rm s}$) records the waves, time-reverses them, and re-emits them into the medium. The field observed at $\boldsymbol{x}_q$ is then exactly $\mathcal{C}(\tau, \boldsymbol{x}_q)$. This time-reversal interpretation of the autocorrelation function (3.5) explains also why the methods used to analyze time reversal [2, 4, 12, 22] are effective in analyzing correlation-based imaging [3, 4, 5].

5.2. Comparisons with virtual source imaging. Another application of correlation-based imaging is to use data recorded by auxiliary passive arrays, usually placed near the reflectors to be imaged, while the main active array provides illumination relatively far from the reflectors. The ambient medium between the illuminating array and the reflectors may be homogeneous or scattering. The illumination provided by the main array is with short, asynchronous, and staggered pulses. The reasons why this type of imaging configuration is interesting and useful are the following:

(1) It can be realized in seismic exploration, in which sources can be put at the surface of the earth and auxiliary receivers may be placed in vertical or horizontal boreholes. It is very difficult to place seismic sources in the boreholes. This kind of imaging configuration, called virtual source imaging, was proposed in seismic imaging by [1, 6, 24, 26].

(2) It can provide images that are essentially unaffected by the scattering inhomogeneities of the medium between the source array and the auxiliary passive array, and may even benefit from them by diversifying the illumination of the reflectors. Further, this will occur even with strong scattering that would make imaging with data from the main, active surface array impossible [14, 15, 16].

Consider an imaging setup in which there is a main array of sources located at $(\boldsymbol{x}_s)_{s=1}^{N_{\rm s}}$ in the plane $z = 0$ and an auxiliary passive array located at $(\boldsymbol{x}_q)_{q=1}^{N_{\rm q}}$ in the plane $z = -L$ (see Figure 6). The data set is then the matrix

$$\big\{u_s(t, \boldsymbol{x}_q)\,,\, t \in [T_s, T_s + T],\, s = 1, \ldots, N_{\rm s},\, q = 1, \ldots, N_{\rm q}\big\},$$

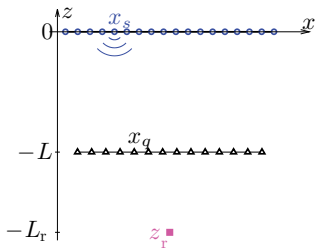

Figure 6. *Use of an auxiliary passive array for imaging through a scattering medium. $\boldsymbol{x}_s$ is a source, $\boldsymbol{x}_q$ is a receiver located below the scattering medium, and $\boldsymbol{z}_r$ is a reflector.*

where $u_s(t, \boldsymbol{x}_q)$ is the signal recorded by the qth receiver when the sth source emits a short pulse of the form $f^\varepsilon(t)$ at a—known or unknown—time T_s:

$$\frac{1}{c^2(\boldsymbol{x})}\frac{\partial^2 u_s}{\partial t^2} - \Delta_{\boldsymbol{x}} u_s = f^\varepsilon(t - T_s)\delta(\boldsymbol{x} - \boldsymbol{x}_s).$$

As in the PSA imaging configurations, we expect that the matrix of cross correlations at the auxiliary array

$$\mathcal{C}_{\rm vs}(\tau, \boldsymbol{x}_q, \boldsymbol{x}_{q'}) = \sum_{s=1}^{N_{\rm s}} \int_{T_s}^{T_s+T-\tau} u_s(t, \boldsymbol{x}_q) u_s(t+\tau, \boldsymbol{x}_{q'}) {\rm d}t, \qquad q, q' = 1, \ldots, N_{\rm q}, \tag{5.1}$$

behaves roughly as if it is the impulse response matrix of the auxiliary array. Indeed, for T large enough, the matrix is given by

$$\mathcal{C}_{\rm vs}(\tau, \boldsymbol{x}_q, \boldsymbol{x}_{q'}) = \frac{1}{2\pi}\sum_{s=1}^{N_{\rm s}} \int_{\mathbb{R}} {\rm d}\omega |\hat{f}^\varepsilon(\omega)|^2 \overline{\hat{G}(\omega, \boldsymbol{x}_q, \boldsymbol{x}_s)} \hat{G}(\omega, \boldsymbol{x}_{q'}, \boldsymbol{x}_s) \exp\big(-i\omega\tau\big), \tag{5.2}$$

where $\hat{G}(\omega, \boldsymbol{x}, \boldsymbol{y})$ is the time-harmonic Green's function of the medium in the presence of the reflector, as in (3.9). If the source array is dense enough so that the sum over s can be replaced by a continuous integral with the source density function $\psi_{\rm s}$, then we find that

$$\begin{aligned} \mathcal{C}_{\rm vs}(\tau, \boldsymbol{x}_q, \boldsymbol{x}_{q'}) = \frac{1}{2\pi}\int_{\mathbb{R}^2} {\rm d}\boldsymbol{y}_\perp \psi_{\rm s}(\boldsymbol{y}_\perp) \\ \times \int_{\mathbb{R}} {\rm d}\omega |\hat{f}^\varepsilon(\omega)|^2 \overline{\hat{G}\big(\omega, \boldsymbol{x}_q, (\boldsymbol{y}_\perp, 0)\big)} \hat{G}\big(\omega, \boldsymbol{x}_{q'}, (\boldsymbol{y}_\perp, 0)\big) \exp\big(-i\omega\tau\big). \end{aligned} \tag{5.3}$$

This shows that a sequence of separated short pulses of the form $f^\varepsilon(t - T_s)$ emitted by the point sources of an array with density function $\psi_{\rm s}(\boldsymbol{y}_\perp)$ in the plane $z = 0$ gives the same illumination and cross correlation as spatially uncorrelated noise sources with power spectral density $|\hat{f}^\varepsilon(\omega)|^2$ and spatial support function $\psi_{\rm s}(\boldsymbol{y}_\perp)$ in the plane $z = 0$.

If the pulse profile $f^\varepsilon(t)$ is of the form (4.1), then the autocorrelation function (3.5) studied in the previous section is the diagonal of the cross correlation matrix (5.3). One can repeat

the same calculations in the high-frequency regime as in the previous section and show that, if there is a point-like reflector at $\boldsymbol{z}_{\rm r}$ below the auxiliary array, then the cross correlation has two peaks at plus or minus the sum of travel times $\mathcal{T}(\boldsymbol{z}_{\rm r},\boldsymbol{x}_q)+\mathcal{T}(\boldsymbol{z}_{\rm r},\boldsymbol{x}_{q'})$. This means that the cross correlation matrix can be used for imaging with Kirchhoff migration,

$$\mathcal{I}_{\rm vs}(\boldsymbol{z}^S)=\sum_{q,q'=1}^{N_{\rm q}}\mathcal{C}_{\rm vs}\big(\mathcal{T}(\boldsymbol{x}_q,\boldsymbol{z}^S)+\mathcal{T}(\boldsymbol{z}^S,\boldsymbol{x}_{q'}),\boldsymbol{x}_q,\boldsymbol{x}_{q'}\big), \tag{5.4}$$

with the travel time $\mathcal{T}$ given by (2.8). Note that, when the auxiliary array is permanent and not synthetic as in the previous sections, then one can get the full cross correlation matrix even with asynchronous and staggered sources, that is, without knowing the emission times, because the signals coming from a source can be recorded by all the receivers at once. A mathematical and numerical analysis of the imaging function (5.4) is given in [14, 15, 16].

6. Numerical illustrations. In this section we present numerical experiments to illustrate the transition from the regime $a_{\rm eff}>a$, in which the resolution properties of active and PSA imaging are equivalent, to the regime $a_{\rm eff}<a$, in which the resolution of PSA imaging is reduced. We consider a two-dimensional situation (see Figures 7(a) and 8(a)) where the following hold:

- There is a point-like reflector at position $\boldsymbol{z}_{\rm r}=(0,-L_{\rm r})$ with $L_{\rm r}=150$, and with reflectivity $\sigma_{\rm r}l_{\rm r}^3=0.05$.
- The successive positions of the antenna are $\boldsymbol{x}_q=(x_q,-L)$ with $L=100$, $x_q=-a/2+a(q-1)/(N_{\rm q}-1)$, $q=1,\ldots,N_{\rm q}$, with $N_{\rm q}=15$ and $a=50$.
- There is a set of $N_{\rm s}=100$ point-like sources at $\boldsymbol{y}_s=(y_s,0)$, $s=1,\ldots,N_{\rm s}$, emitting independent noise signals with Gaussian statistics, mean zero, and power spectral density

$$\hat{F}(\omega)=\omega^2\exp(-\omega^2).$$

Therefore the central frequency is $\omega_0=1$, and the central wavelength is 2π. The noise source locations $(y_s)_{s=1}^{N_{\rm s}}$ are randomly distributed on the interval $[-b/2,b/2]$ in the plane $z=0$. We address two different values for the diameter b of the noise source region: $b=180$ (Figure 7) and $b=60$ (Figure 8). By (2.9), we have $a_{\rm eff}=60$ in the first case and $a_{\rm eff}=20$ in the second case.

We want to compare the images produced by the PSA migration function (2.7) and those produced by the ASA function (4.4).

The PSA function uses the autocorrelation functions of the ambient noise signals recorded by the passive antenna at its $N_{\rm q}$ successive positions:

$$\mathcal{C}(\tau,\boldsymbol{x}_q)=\frac{1}{2\pi N_{\rm s}}\sum_{s=1}^{N_{\rm s}}\int_{\mathbb{R}}{\rm d}\omega\hat{F}(\omega)|\hat{G}\big(\omega,\boldsymbol{x}_q,\boldsymbol{y}_s\big)|^2\exp\big(-i\omega\tau\big),\qquad q=1,\ldots,N_{\rm q},$$

where $\hat{G}$ is given by (3.9) in terms of the two-dimensional homogeneous Green's function

$$\hat{G}_0(\omega,\boldsymbol{x},\boldsymbol{y})=\frac{i}{4}H_0^{(1)}\left(\frac{\omega}{c_0}|\boldsymbol{x}-\boldsymbol{y}|\right),$$

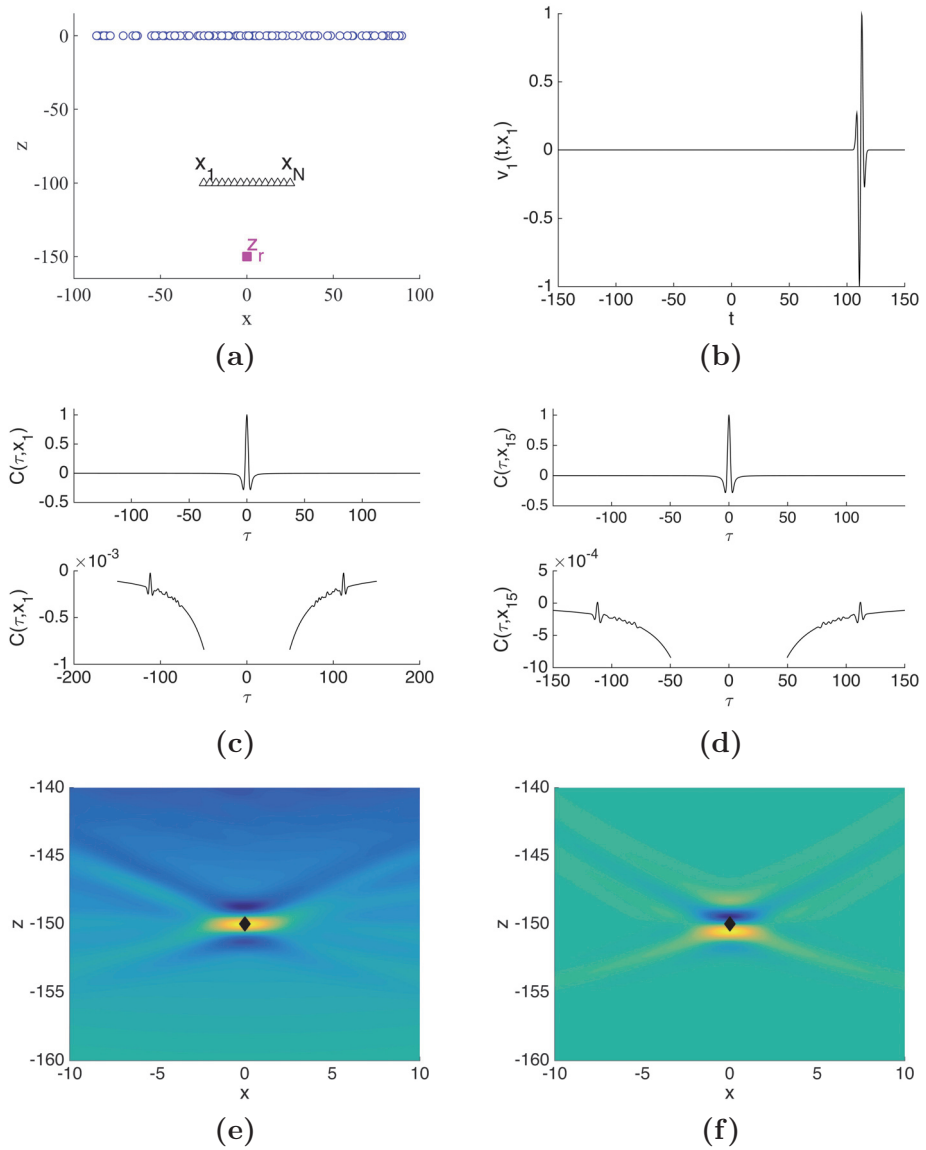

Figure 7. *ASA and PSA images. Here the diameter of the noise source region is* $b = 180$. *Geometric setup* (a). *Signal backscattered at the active antenna at* $\boldsymbol{x}_1$ (b). *Statistical autocorrelation functions at* $\boldsymbol{x}_1$ (c) *and* $\boldsymbol{x}_{15}$ (d). *PSA migration function* (e). *ASA function* (f).

with $H_0^{(1)}$ the Hankel function of the first kind and of order zero.

The ASA function uses the backscattered signals emitted and recorded by the active antenna at its N_{q} successive positions:

$$v_q(t,\boldsymbol{x}_q) = \frac{1}{2\pi}\int_{\mathbb{R}} \mathrm{d}\omega \sqrt{\hat{F}(\omega)}\frac{\omega^2}{c_0^2}\sigma_{\mathrm{r}} l_{\mathrm{r}}^3 \hat{G}_0(\omega,\boldsymbol{x}_q,\boldsymbol{z}_{\mathrm{r}})^2 \exp\big(-i\omega t\big), \qquad q = 1,\ldots,N_{\mathrm{q}}.$$

Figures 7 and 8 are organized in the same way. The only difference between them is the

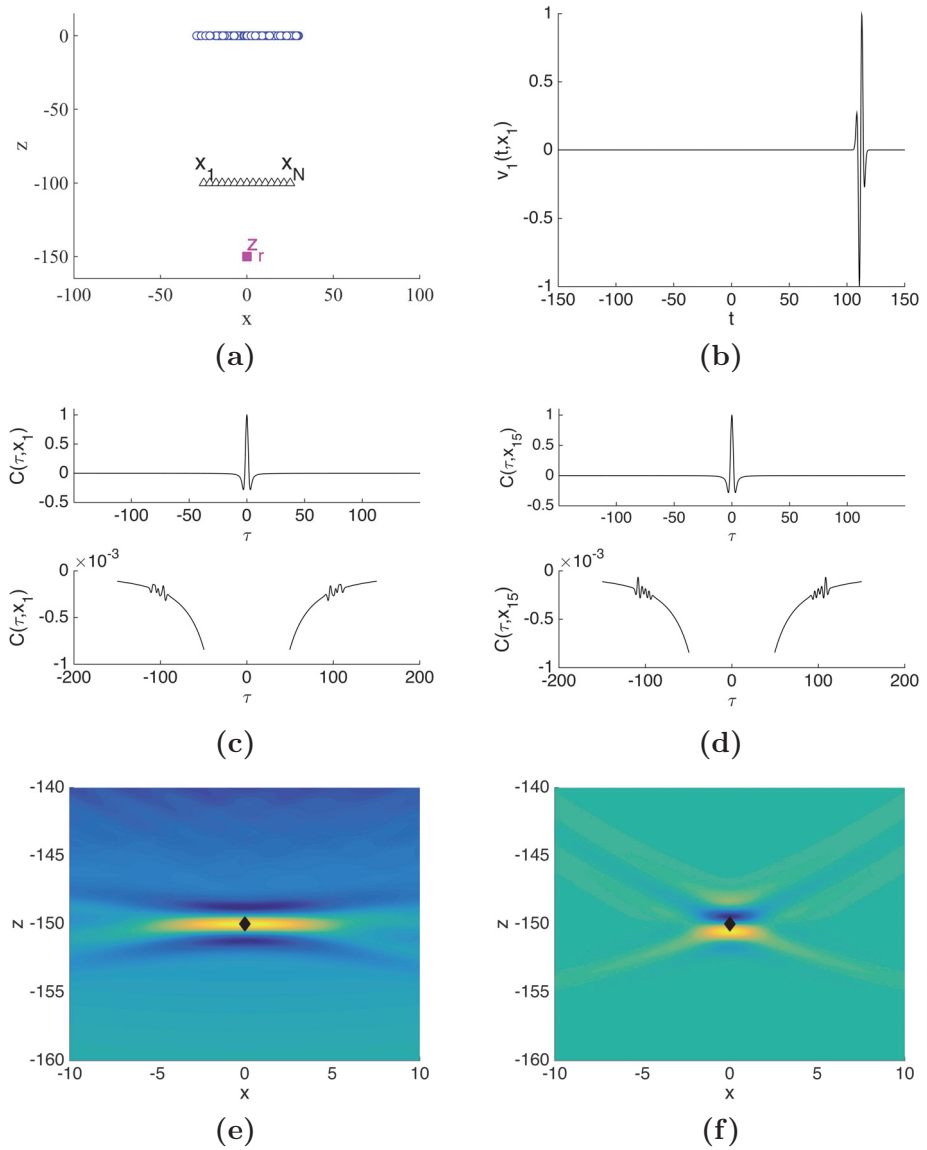

Figure 8. *Active and passive synthetic aperture images. Here the diameter of the noise source region is* $b = 60$.

diameter b of the noise source region:

• In (a), the geometric setup is plotted. The circles are the noise sources, the triangles are the successive positions of the antenna, and the square is the reflector.

• In (b), the backscattered signal recorded by the active antenna at $\boldsymbol{x}_1$ is plotted: one can clearly identify a peak at a time equal to twice the travel time from $\boldsymbol{x}_1$ to $\boldsymbol{z}_{\rm r}$.

• In (c) and (d), the statistical autocorrelation functions of the ambient noise signals recorded at $\boldsymbol{x}_1$ (c) and at $\boldsymbol{x}_{15}$ (d) are plotted. The top pictures show that the main contribution is the background autocorrelation centered at $\tau = 0$ and does not depend on the reflector.

The bottom pictures are zooms that show the contributions of the reflector additionally to the tails of the main contributions. Note that the tails of the main contribution decay slowly, as a power law, which is characteristic of the two-dimensional situation in which the time-dependent Green's function has a slow decay. If one were addressing a three-dimensional configuration, one would not see such tails.

• In (e) and (f), the PSA function (e) and the ASA function (f) are plotted. Here we can see the differences between Figures 7 and 8. In Figure 7, we have $b = 180$ and therefore $a_{\text{eff}} = 60 > 50 = a$, so that the resolution of the PSA and ASA functions is equivalent, both in the transverse and longitudinal directions. (The difference in the longitudinal profiles comes from the fact that the order of the derivative of the function F is different in the expressions of the point spread functions of the two imaging functions; see (3.22) and (4.6) in the three-dimensional setup.) In Figure 8, we have $b = 60$ and therefore $a_{\text{eff}} = 20 < 50 = a$, so that the transverse resolution of the PSA function is clearly reduced compared to that of the ASA function.

7. Conclusion.

In this paper we have presented and analyzed a passive synthetic aperture imaging function that exploits the signals recorded by a moving receiver, which are generated by distant noise sources. The analysis of this imaging method is done in a homogeneous medium, in a high-frequency regime, and we have quantified the dependence of the resolution on the diameter of the noise source region and the diameter of the synthetic receiver array. We have shown that the resolution of PSA imaging is essentially equivalent to that of the usual ASA imaging, provided that the illumination in the passive case is sufficiently rich.

Appendix A. Proof of Proposition 3.1.

We follow the arguments in [13]. By the stationarity (in time) of the process $n^\varepsilon(t, \boldsymbol{x}_\perp)$, the product $u(t, \boldsymbol{x}_1)u(t+\tau, \boldsymbol{x}_2)$ is itself a stationary random process in t. Therefore the mean of $\mathcal{C}_T$ is independent of T and is given by

$$\langle \mathcal{C}_T(\tau, \boldsymbol{x}_q)\rangle = \langle u(0, \boldsymbol{x}_q)u(\tau, \boldsymbol{x}_q)\rangle\,.$$

Using (3.2), we get the following integral representation for the average of the autocorrelation function:

$$\langle \mathcal{C}_T(\tau, \boldsymbol{x}_q)\rangle = \iint_{\mathbb{R}^2\times\mathbb{R}^2} \mathrm{d}\boldsymbol{y}_\perp \mathrm{d}\boldsymbol{y}'_\perp \iint_{\mathbb{R}\times\mathbb{R}} \mathrm{d}s'\mathrm{d}s G(s, \boldsymbol{x}_q, (\boldsymbol{y}_\perp, 0))G(s', \boldsymbol{x}_q, (\boldsymbol{y}'_\perp, 0)) \times \left\langle n^\varepsilon(-s, \boldsymbol{y}_\perp)n^\varepsilon(\tau - s', \boldsymbol{y}'_\perp)\right\rangle.$$

Using the form (2.4) of the autocorrelation function of the noise sources, we obtain

$$\langle \mathcal{C}_T(\tau, \boldsymbol{x}_q)\rangle = \int_{\mathbb{R}^2} \mathrm{d}\boldsymbol{y}_\perp \iint_{\mathbb{R}\times\mathbb{R}} \mathrm{d}s\mathrm{d}s' G(s, \boldsymbol{x}_q, (\boldsymbol{y}_\perp, 0))G(\tau + s + s', \boldsymbol{x}_q, (\boldsymbol{y}_\perp, 0)) \times F^\varepsilon(s')\psi_{\mathrm{s}}(\boldsymbol{y}_\perp),$$

which in the Fourier domain is (3.5):

$$\langle \mathcal{C}_T(\tau, \boldsymbol{x}_q)\rangle = \frac{1}{2\pi}\int_{\mathbb{R}} \mathrm{d}\omega \hat{F}^\varepsilon(\omega) \int_{\mathbb{R}^2} \mathrm{d}\boldsymbol{y}_\perp \psi_{\mathrm{s}}(\boldsymbol{y}_\perp)|\hat{G}\big(\omega, \boldsymbol{x}_q, (\boldsymbol{y}_\perp, 0)\big)|^2 \exp\big(-i\omega\tau\big).$$

This completes the proof of the first item of the proposition.

Note that, using the form (3.7) of the power spectral density, we can also write

$$\langle \mathcal{C}_T(\tau,\boldsymbol{x}_q)\rangle = \frac{1}{2\pi}\int_{\mathbb{R}} \mathrm{d}\omega \hat{F}(\omega)\int_{\mathbb{R}^2}\mathrm{d}\boldsymbol{y}_\perp \psi_{\mathrm{s}}(\boldsymbol{y}_\perp)\left|\hat{G}\left(\frac{\omega}{\varepsilon},\boldsymbol{x}_q,(\boldsymbol{y}_\perp,0)\right)\right|^2 \exp\left(-i\frac{\omega}{\varepsilon}\tau\right),$$

which shows that the statistical autocorrelation function is of order one in the regime $\varepsilon \to 0$.

In order to prove the second item of the proposition, that is, the self-averaging property of the autocorrelation function $\mathcal{C}_T$, we compute its variance. This calculation is carried out at the end of this section; it is long but explicit as the Gaussian property of the noise sources allows us to write their fourth-order moments as sums of products of second-order moments. It shows that the variance goes to zero as $T/\varepsilon \to \infty$, that is, the empirical autocorrelation converges to its expectation in the mean-squared sense, and therefore in probability

$$\mathbb{P}\Big(\big|\mathcal{C}_T(\tau,\boldsymbol{x}_q) - \langle \mathcal{C}_T(\tau,\boldsymbol{x}_q)\rangle\,\big| \ge \delta\Big) \le \frac{\mathrm{Var}\big(\mathcal{C}_T(\tau,\boldsymbol{x}_q)\big)}{\delta^2},$$

by Chebyshev's inequality.

The principle of the computation of the variance of $\mathcal{C}_T$ is the following. We first write the variance of $\mathcal{C}_T$ as a multiple integral which involves the fourth-order moment of the random process n^ε. Since n^ε is Gaussian, this fourth-order moment can be written as the sum of products of second-order moments, which makes the computation tractable. Using (3.2) and (2.6), we find that the variance of the empirical autocorrelation function is

$$\begin{aligned}
&\mathrm{Var}\big(\mathcal{C}_T(\tau,\boldsymbol{x}_q)\big)\\
&= \frac{1}{(T-\tau)^2}\int_{T_q}^{T_q+T-\tau}\int_{T_q}^{T_q+T-\tau}\mathrm{d}t\mathrm{d}t'\int \mathrm{d}s\mathrm{d}s'\mathrm{d}u\mathrm{d}u'\int \mathrm{d}\boldsymbol{y}_{1_\perp}\mathrm{d}\boldsymbol{y}'_{1_\perp}\mathrm{d}\boldsymbol{y}_{2_\perp}\mathrm{d}\boldsymbol{y}'_{2_\perp}\\
&\quad\times G(s,\boldsymbol{x}_q,(\boldsymbol{y}_{1_\perp},0))G(u+\tau,\boldsymbol{x}_q,(\boldsymbol{y}_{2_\perp},0))G(s',\boldsymbol{x}_q,(\boldsymbol{y}'_{1_\perp},0))G(u'+\tau,\boldsymbol{x}_q,(\boldsymbol{y}'_{2_\perp},0))\\
&\quad\times\Big(\big\langle n^\varepsilon(t-s,\boldsymbol{y}_{1_\perp})n^\varepsilon(t-u,\boldsymbol{y}_{2_\perp})n^\varepsilon(t'-s',\boldsymbol{y}'_{1_\perp})n^\varepsilon(t'-u',\boldsymbol{y}'_{2_\perp})\big\rangle\\
&\qquad - \langle n^\varepsilon(t-s,\boldsymbol{y}_{1_\perp})n^\varepsilon(t-u,\boldsymbol{y}_{2_\perp})\rangle\big\langle n^\varepsilon(t'-s',\boldsymbol{y}'_{1_\perp})n^\varepsilon(t'-u',\boldsymbol{y}'_{2_\perp})\big\rangle\Big).
\end{aligned}\tag{A.1}$$

The product of second-order moments of the random process n^ε is

$$\begin{aligned}
&\langle n^\varepsilon(t-s,\boldsymbol{y}_{1_\perp})n^\varepsilon(t-u,\boldsymbol{y}_{2_\perp})\rangle\big\langle n^\varepsilon(t'-s',\boldsymbol{y}'_{1_\perp})n^\varepsilon(t'-u',\boldsymbol{y}'_{2_\perp})\big\rangle\\
&\quad = F^\varepsilon(s-u)F^\varepsilon(s'-u')\psi_{\mathrm{s}}(\boldsymbol{y}_{1_\perp})\delta(\boldsymbol{y}_{1_\perp}-\boldsymbol{y}_{2_\perp})\psi_{\mathrm{s}}(\boldsymbol{y}'_{1_\perp})\delta(\boldsymbol{y}'_{1_\perp}-\boldsymbol{y}'_{2_\perp}).
\end{aligned}$$

The fourth-order moment of the Gaussian random process n^ε is

$$\begin{aligned}
&\big\langle n^\varepsilon(t-s,\boldsymbol{y}_{1_\perp})n^\varepsilon(t-u,\boldsymbol{y}_{2_\perp})n^\varepsilon(t'-s',\boldsymbol{y}'_{1_\perp})n^\varepsilon(t'-u',\boldsymbol{y}'_{2_\perp})\big\rangle\\
&\quad = F^\varepsilon(s-u)F^\varepsilon(s'-u')\psi_{\mathrm{s}}(\boldsymbol{y}_{1_\perp})\delta(\boldsymbol{y}_{1_\perp}-\boldsymbol{y}_{2_\perp})\psi_{\mathrm{s}}(\boldsymbol{y}'_{1_\perp})\delta(\boldsymbol{y}'_{1_\perp}-\boldsymbol{y}'_{2_\perp})\\
&\qquad + F^\varepsilon(t-t'-s+s')F^\varepsilon(t-t'-u+u')\psi_{\mathrm{s}}(\boldsymbol{y}_{1_\perp})\delta(\boldsymbol{y}_{1_\perp}-\boldsymbol{y}'_{1_\perp})\psi_{\mathrm{s}}(\boldsymbol{y}_{2_\perp})\delta(\boldsymbol{y}_{2_\perp}-\boldsymbol{y}'_{2_\perp})\\
&\qquad + F^\varepsilon(t-t'-s+u')F^\varepsilon(t-t'-u+s')\psi_{\mathrm{s}}(\boldsymbol{y}_{1_\perp})\delta(\boldsymbol{y}_{1_\perp}-\boldsymbol{y}'_{2_\perp})\psi_{\mathrm{s}}(\boldsymbol{y}_{2_\perp})\delta(\boldsymbol{y}'_{1_\perp}-\boldsymbol{y}_{2_\perp}).
\end{aligned}$$

Consequently, we have that, for any $T > 0$,

$$\begin{aligned}\frac{1}{T^2}\int_0^T\int_0^T \mathrm{d}t\mathrm{d}t'\Big(&\big\langle n^\varepsilon(t-s,\boldsymbol{y}_{1_\perp})n^\varepsilon(t-u,\boldsymbol{y}_{2_\perp})n^\varepsilon(t'-s',\boldsymbol{y}'_{1_\perp})n^\varepsilon(t'-u',\boldsymbol{y}'_{2_\perp})\big\rangle\\ &-\langle n^\varepsilon(t-s,\boldsymbol{y}_{1_\perp})n^\varepsilon(t-u,\boldsymbol{y}_{2_\perp})\rangle\big\langle n^\varepsilon(t'-s',\boldsymbol{y}'_{1_\perp})n^\varepsilon(t'-u',\boldsymbol{y}'_{2_\perp})\big\rangle\Big)\\ &= S_T(s-s',u-u')\psi_{\mathrm{s}}(\boldsymbol{y}_{1_\perp})\delta(\boldsymbol{y}_{1_\perp}-\boldsymbol{y}'_{1_\perp})\psi_{\mathrm{s}}(\boldsymbol{y}_{2_\perp})\delta(\boldsymbol{y}_{2_\perp}-\boldsymbol{y}'_{2_\perp})\\ &\quad + S_T(s-u',u-s')\psi_{\mathrm{s}}(\boldsymbol{y}_{1_\perp})\delta(\boldsymbol{y}_{1_\perp}-\boldsymbol{y}'_{2_\perp})\psi_{\mathrm{s}}(\boldsymbol{y}_{2_\perp})\delta(\boldsymbol{y}'_{1_\perp}-\boldsymbol{y}_{2_\perp})\,,\end{aligned} \tag{A.2}$$

where

$$\begin{aligned}S_T(s,u) &= \frac{1}{T^2}\int_0^T \mathrm{d}t\int_0^T \mathrm{d}t' F^\varepsilon(t-t'-s)F^\varepsilon(t-t'-u)\\ &= \frac{1}{4\pi^2}\int \mathrm{d}\omega\mathrm{d}\omega'\hat{F}^\varepsilon(\omega)\hat{F}^\varepsilon(\omega')\mathrm{sinc}^2\left(\frac{(\omega-\omega')T}{2}\right)e^{-i\omega s+i\omega' u}\,.\end{aligned}$$

Substituting into (A.1), we obtain the following expression for the variance of the empirical autocorrelation function:

$$\begin{aligned}\mathrm{Var}\big(\mathcal{C}_T(\tau,\boldsymbol{x}_q)\big) = \ &\frac{1}{4\pi^2}\int \mathrm{d}\boldsymbol{y}_{1_\perp}\mathrm{d}\boldsymbol{y}_{2_\perp}\psi_{\mathrm{s}}(\boldsymbol{y}_{1_\perp})\psi_{\mathrm{s}}(\boldsymbol{y}_{2_\perp})\int \mathrm{d}\omega\mathrm{d}\omega'\hat{F}^\varepsilon(\omega)\hat{F}^\varepsilon(\omega')\\ &\times\big|\hat{G}(\omega,\boldsymbol{x}_q,\boldsymbol{y}_{1_\perp})\big|^2\big|\hat{G}(\omega',\boldsymbol{x}_q,\boldsymbol{y}_{2_\perp})\big|^2\mathrm{sinc}^2\left(\frac{(\omega-\omega')(T-\tau)}{2}\right)\left[1+e^{-i(\omega'+\omega)\tau}\right].\end{aligned}$$

Using the form (3.7) of the power spectral density, we can also write

$$\begin{aligned}\mathrm{Var}\big(\mathcal{C}_T(\tau,\boldsymbol{x}_q)\big) = \ &\frac{1}{4\pi^2}\int \mathrm{d}\boldsymbol{y}_{1_\perp}\mathrm{d}\boldsymbol{y}_{2_\perp}\psi_{\mathrm{s}}(\boldsymbol{y}_{1_\perp})\psi_{\mathrm{s}}(\boldsymbol{y}_{2_\perp})\int \mathrm{d}\omega\mathrm{d}\omega'\hat{F}(\omega)\hat{F}(\omega')\\ &\times\left|\hat{G}\left(\frac{\omega}{\varepsilon},\boldsymbol{x}_q,\boldsymbol{y}_{1_\perp}\right)\right|^2\left|\hat{G}\left(\frac{\omega'}{\varepsilon},\boldsymbol{x}_q,\boldsymbol{y}_{2_\perp}\right)\right|^2\mathrm{sinc}^2\left(\frac{(\omega-\omega')(T-\tau)}{2\varepsilon}\right)\left[1+e^{-i\frac{\omega'+\omega}{\varepsilon}\tau}\right].\end{aligned}$$

Using the fact that $\int \mathrm{sinc}^2 s\mathrm{d}s = \pi$, we can see that $M\mathrm{sinc}^2[M(s-s')]$ behaves like $\pi\delta(s-s')$ as $M\to\infty$. Taking the limit $T\to\infty$, we get that the variance is of order $\varepsilon/(T-\tau)$:

$$\begin{aligned}\frac{T-\tau}{\varepsilon}\mathrm{Var}\big(\mathcal{C}_T(\tau,\boldsymbol{x}_q)\big) \overset{T\to\infty}{\longrightarrow} &\frac{1}{2\pi}\int \mathrm{d}\omega\hat{F}(\omega)^2\left[1+e^{-2i\frac{\omega}{\varepsilon}\tau}\right]\\ &\times\left[\int \mathrm{d}\boldsymbol{y}_\perp\psi_{\mathrm{s}}(\boldsymbol{y}_\perp)\left|\hat{G}\left(\frac{\omega}{\varepsilon},\boldsymbol{x}_q,\boldsymbol{y}_\perp\right)\right|^2\right]^2,\end{aligned}$$

which shows that the relative fluctuations of the autocorrelation function are of order $\sqrt{\varepsilon/(T-\tau)}$.

Appendix B. Proof of Proposition 3.2. We consider the first term $\Delta\mathcal{C}_{\mathrm{I}}$ defined by (3.14). Using the explicit expression of the homogeneous Green's function,

$$\hat{G}_0(\omega,\boldsymbol{x},\boldsymbol{y}) = \frac{1}{4\pi|\boldsymbol{x}-\boldsymbol{y}|}\exp\big(i\omega\mathcal{T}(\boldsymbol{x},\boldsymbol{y})\big), \qquad \mathcal{T}(\boldsymbol{x},\boldsymbol{y}) = \frac{|\boldsymbol{x}-\boldsymbol{y}|}{c_0}, \tag{B.1}$$

it can be written as

$$\Delta\mathcal{C}_{\rm I}(\tau,\boldsymbol{x}_q)=\frac{\sigma_{\rm r} l_{\rm r}^3}{2^7\pi^4 c_0^2\varepsilon^2}\int_{\mathbb{R}^2}{\rm d}\boldsymbol{y}_\perp\int_{\mathbb{R}}{\rm d}\omega\frac{\psi_{\rm s}(\boldsymbol{y}_\perp)\omega^2\hat{F}(\omega)}{|\boldsymbol{x}_q-\boldsymbol{z}_{\rm r}||\boldsymbol{z}_{\rm r}-(\boldsymbol{y}_\perp,0)||\boldsymbol{x}_q-(\boldsymbol{y}_\perp,0)|}\\ \times\exp\left(i\frac{\Phi_{\rm I}(\boldsymbol{y}_\perp,\omega)}{\varepsilon}\right),$$

where the rapid phase is

$$\Phi_{\rm I}(\boldsymbol{y}_\perp,\omega)=\omega\Big[\mathcal{T}(\boldsymbol{x}_q,(\boldsymbol{y}_\perp,0))-\mathcal{T}(\boldsymbol{x}_q,\boldsymbol{z}_{\rm r})-\mathcal{T}(\boldsymbol{z}_{\rm r},(\boldsymbol{y}_\perp,0))-\tau\Big].$$

In order to identify the dominant contributions of the first term with the rapid phase $\Phi_{\rm I}$ we apply the stationary phase method. The stationary points satisfy the two conditions

$$\partial_\omega\big(\Phi_{\rm I}(\omega,\boldsymbol{y}_\perp)\big)=0,\qquad \nabla_{\boldsymbol{y}_\perp}\big(\Phi_{\rm I}(\omega,\boldsymbol{y}_\perp)\big)=\boldsymbol{0},$$

which means

$$\mathcal{T}(\boldsymbol{x}_q,(\boldsymbol{y}_\perp,0))-\mathcal{T}(\boldsymbol{x}_q,\boldsymbol{z}_{\rm r})-\mathcal{T}(\boldsymbol{z}_{\rm r},(\boldsymbol{y}_\perp,0))-\tau=0,\\ \nabla_{\boldsymbol{y}_\perp}\mathcal{T}(\boldsymbol{x}_q,(\boldsymbol{y}_\perp,0))-\nabla_{\boldsymbol{y}_\perp}\mathcal{T}(\boldsymbol{z}_{\rm r},(\boldsymbol{y}_\perp,0))=0.$$

The second condition means

$$\frac{\boldsymbol{y}_\perp-\boldsymbol{x}_{q_\perp}}{\sqrt{L^2+|\boldsymbol{x}_{q_\perp}-\boldsymbol{y}_\perp|^2}}-\frac{\boldsymbol{y}_\perp-\boldsymbol{z}_{{\rm r}_\perp}}{\sqrt{L_{\rm r}^2+|\boldsymbol{z}_{{\rm r}_\perp}-\boldsymbol{y}_\perp|^2}}=0,$$

which can be solved as

$$\boldsymbol{y}_\perp=\boldsymbol{Y}_\perp(\boldsymbol{x}_{q_\perp}),$$

with $\boldsymbol{Y}_\perp$ defined as (3.18), that is, the intersection of the ray going through $\boldsymbol{x}_q$ and $\boldsymbol{z}_{\rm r}$ with the noise source plane $z=0$. And then the first condition reads $\tau=-2\mathcal{T}(\boldsymbol{x}_q,\boldsymbol{z}_{\rm r})$.

We introduce the unit vector

$$\hat{\boldsymbol{g}}_1=\frac{\boldsymbol{z}_{{\rm r}_\perp}-\boldsymbol{x}_{q_\perp}}{|\boldsymbol{z}_{{\rm r}_\perp}-\boldsymbol{x}_{q_\perp}|}$$

and complete it with another unit vector $\hat{\boldsymbol{g}}_2\in\mathbb{R}^2$ so that $(\hat{\boldsymbol{g}}_1,\hat{\boldsymbol{g}}_2)$ is an orthonormal basis of $\mathbb{R}^2$. We make the change of variables

$$\boldsymbol{y}_\perp=\boldsymbol{Y}_\perp(\boldsymbol{x}_{q_\perp})+\sqrt{\varepsilon}|\boldsymbol{z}_{\rm r}-\boldsymbol{x}_q|(s_1\hat{\boldsymbol{g}}_1+s_2\hat{\boldsymbol{g}}_2),$$

whose Jacobian is $\varepsilon|\boldsymbol{z}_{\rm r}-\boldsymbol{x}_q|^2$. We also parameterize the lag time τ around minus twice the travel time from the receiver to the reflector:

$$\tau=-2\mathcal{T}(\boldsymbol{x}_q,\boldsymbol{z}_{\rm r})+\varepsilon\tau_0.$$

By carrying out Taylor expansions, we get

$$\frac{\psi_{\rm s}(\boldsymbol{y}_\perp)}{|\boldsymbol{x}_q-\boldsymbol{z}_{\rm r}||\boldsymbol{z}_{\rm r}-(\boldsymbol{y}_\perp,0)||\boldsymbol{x}_q-(\boldsymbol{y}_\perp,0)|}=\frac{\psi_{\rm s}(\boldsymbol{Y}_\perp(\boldsymbol{x}_{q_\perp}))(L_{\rm r}-L)^2}{|\boldsymbol{x}_q-\boldsymbol{z}_{\rm r}|^3L_{\rm r}L}\big[1+O(\varepsilon^{1/2})\big],$$

$$\Phi_{\rm I}=\varepsilon\omega\left[\frac{(L_{\rm r}-L)^2|\boldsymbol{z}_{\rm r}-\boldsymbol{x}_q|}{2c_0L_{\rm r}L}\left(s_1^2\frac{(L_{\rm r}-L)^2}{|\boldsymbol{z}_{\rm r}-\boldsymbol{x}_q|^2}+s_2^2\right)-\tau_0\right]\big[1+O(\varepsilon^{1/2})\big].$$

Using the second expansion and the identity $\int \exp(is^2/2)\mathrm{d}s = \sqrt{2\pi}\exp(i\pi/4)$, we find that, as $\varepsilon \to 0$,

$$\int_{\mathbb{R}^2} \exp\Big(i\frac{\Phi_{\mathrm{I}}}{\varepsilon}\Big)\mathrm{d}s_1\mathrm{d}s_2 = \frac{2i\pi c_0 L_{\mathrm{r}} L}{(L_{\mathrm{r}}-L)^3\omega}\exp(-i\omega\tau_0).$$

Using these relations, we finally obtain

$$\begin{aligned}\Delta\mathcal{C}_{\mathrm{I}}(\tau,\boldsymbol{x}_q) &= \frac{\sigma_{\mathrm{r}} l_{\mathrm{r}}^3}{2^6\pi^3 c_0\varepsilon}\frac{\psi_{\mathrm{s}}(\boldsymbol{Y}_\perp(\boldsymbol{x}_{q_\perp}))}{(L_{\mathrm{r}}-L)|\boldsymbol{z}_{\mathrm{r}}-\boldsymbol{x}_q|}\left[\int_{\mathbb{R}}\mathrm{d}\omega\hat{F}(\omega)i\omega\exp(-i\omega\tau_0)\right]\\ &= \frac{\sigma_{\mathrm{r}} l_{\mathrm{r}}^3}{2^5\pi^2 c_0\varepsilon}\frac{\mathcal{K}(\boldsymbol{x}_q,\boldsymbol{z}_{\mathrm{r}})}{|\boldsymbol{z}_{\mathrm{r}}-\boldsymbol{x}_q|^2}\left[\frac{1}{2\pi}\int_{\mathbb{R}}\mathrm{d}\omega\hat{F}(\omega)i\omega\exp(-i\omega\tau_0)\right],\end{aligned}$$

which gives

$$\Delta\mathcal{C}_{\mathrm{I}}(\tau,\boldsymbol{x}_q) = -\frac{\sigma_{\mathrm{r}} l_{\mathrm{r}}^3}{2^5\pi^2 c_0\varepsilon}\frac{\mathcal{K}(\boldsymbol{x}_q,\boldsymbol{z}_{\mathrm{r}})}{|\boldsymbol{z}_{\mathrm{r}}-\boldsymbol{x}_q|^2}\partial_\tau F(\tau_0),$$

with $\mathcal{K}$ defined by (3.17). Computing in the same way the expression of $\Delta\mathcal{C}_{\mathrm{II}}(\tau,\boldsymbol{x}_q)$, we obtain the desired result.

Appendix C. Proof of Proposition 3.3. We consider (3.19). It is the sum of two contributions coming from $\Delta\mathcal{C}_{\mathrm{I}}$ and $\Delta\mathcal{C}_{\mathrm{II}}$. Using the fact that $\Delta\mathcal{C}(\tau,\boldsymbol{x}) = \Delta\mathcal{C}(-\tau,\boldsymbol{x})$, we can write

$$\mathcal{I}_{\mathrm{psa}}(\boldsymbol{z}^S) = \mathcal{I}_{\mathrm{I}+}(\boldsymbol{z}^S) + \mathcal{I}_{\mathrm{II}+}(\boldsymbol{z}^S) + \mathcal{I}_{\mathrm{I}-}(\boldsymbol{z}^S) + \mathcal{I}_{\mathrm{II}-}(\boldsymbol{z}^S),$$

where

$$\mathcal{I}_{\mathrm{I}\pm}(\boldsymbol{z}^S) = \frac{1}{2}\int_{\mathbb{R}^2}\mathrm{d}\boldsymbol{x}_\perp\psi_{\mathrm{q}}(\boldsymbol{x}_\perp)\Delta\mathcal{C}_{\mathrm{I}}\big(\pm 2\mathcal{T}((\boldsymbol{x}_\perp,-L),\boldsymbol{z}^S),(\boldsymbol{x}_\perp,-L)\big)$$

and

$$\mathcal{I}_{\mathrm{II}\pm}(\boldsymbol{z}^S) = \frac{1}{2}\int_{\mathbb{R}^2}\mathrm{d}\boldsymbol{x}_\perp\psi_{\mathrm{q}}(\boldsymbol{x}_\perp)\Delta\mathcal{C}_{\mathrm{II}}\big(\pm 2\mathcal{T}((\boldsymbol{x}_\perp,-L),\boldsymbol{z}^S),(\boldsymbol{x}_\perp,-L)\big).$$

Let us consider the first term $\mathcal{I}_{\mathrm{I}-}$. By using the explicit form of the Green's function (B.1), it can be written as

$$\begin{aligned}\mathcal{I}_{\mathrm{I}-}(\boldsymbol{z}^S) = \frac{\sigma_{\mathrm{r}} l_{\mathrm{r}}^3}{2^8\pi^4 c_0^2\varepsilon^2}\int_{\mathbb{R}^2}\mathrm{d}\boldsymbol{x}_\perp\int_{\mathbb{R}}\mathrm{d}\omega\int_{\mathbb{R}^2}\mathrm{d}\boldsymbol{y}_\perp\\ \times\frac{\omega^2\hat{F}(\omega)\psi_{\mathrm{q}}(\boldsymbol{x}_\perp)\psi_{\mathrm{s}}(\boldsymbol{y}_\perp)}{|(\boldsymbol{y}_\perp,0)-(\boldsymbol{x}_\perp,-L)||(\boldsymbol{x}_\perp,-L)-\boldsymbol{z}_{\mathrm{r}}||\boldsymbol{z}_{\mathrm{r}}-(\boldsymbol{y}_\perp,0)|}\exp\left(i\frac{\Phi(\omega,\boldsymbol{y}_\perp,\boldsymbol{x}_\perp)}{\varepsilon}\right),\end{aligned}$$

where the rapid phase is

$$\begin{aligned}\Phi(\omega,\boldsymbol{y}_\perp,\boldsymbol{x}_\perp) = \omega\Big[\mathcal{T}((\boldsymbol{x}_\perp,-L),(\boldsymbol{y}_\perp,0)) - \mathcal{T}((\boldsymbol{x}_\perp,-L),\boldsymbol{z}_{\mathrm{r}}) - \mathcal{T}(\boldsymbol{z}_{\mathrm{r}},(\boldsymbol{y}_\perp,0))\\ + 2\mathcal{T}((\boldsymbol{x}_\perp,-L),\boldsymbol{z}^S)\Big].\end{aligned}$$

In order to identify the dominant contributions, we apply the stationary phase method. The stationary points satisfy the three conditions

$$\partial_\omega\big(\Phi(\omega,\boldsymbol{y}_\perp,\boldsymbol{x}_\perp)\big) = 0, \qquad \nabla_{\boldsymbol{y}_\perp}\big(\Phi(\omega,\boldsymbol{y}_\perp,\boldsymbol{x}_\perp)\big) = \boldsymbol{0}, \qquad \nabla_{\boldsymbol{x}_\perp}\big(\Phi(\omega,\boldsymbol{y}_\perp,\boldsymbol{x}_\perp)\big) = \boldsymbol{0}.$$

The second condition means

$$\boldsymbol{y}_\perp = \boldsymbol{Y}_\perp(\boldsymbol{x}_\perp),$$

with $\boldsymbol{Y}_\perp$ defined as in (3.18). And then the two other conditions are fulfilled, provided that $\boldsymbol{z}^S = \boldsymbol{z}_{\rm r}$.

We parameterize the search point $\boldsymbol{z}^S$ around the reflector location $\boldsymbol{z}_{\rm r}$:

$$\boldsymbol{z}^S = \boldsymbol{z}_{\rm r} + \varepsilon \boldsymbol{z}.$$

By carrying out Taylor expansions as in the proof of Proposition 3.2 and using also the Taylor expansion

$$|(\boldsymbol{x}_\perp, -L) - \boldsymbol{z}^S| = |(\boldsymbol{x}_\perp, -L) - \boldsymbol{z}_{\rm r}| \left[1 - \varepsilon \frac{\boldsymbol{z}\cdot((\boldsymbol{x}_\perp, -L) - \boldsymbol{z}_{\rm r})}{|(\boldsymbol{x}_\perp, -L) - \boldsymbol{z}_{\rm r}|^2} + O(\varepsilon^2)\right],$$

we find

$$\begin{aligned}\mathcal{I}_{\rm I-}(\boldsymbol{z}^S) = {}& \frac{\sigma_{\rm r} l_{\rm r}^3}{2^8\pi^4 c_0^2 \varepsilon} \int_{\mathbb{R}^2} {\rm d}\boldsymbol{x}_\perp \int_{\mathbb{R}} {\rm d}\omega \frac{\omega^2 \hat{F}(\omega)\psi_{\rm q}(\boldsymbol{x}_\perp)\psi_{\rm s}(\boldsymbol{Y}_\perp(\boldsymbol{x}_\perp))(L_{\rm r}-L)^2}{|(\boldsymbol{x}_\perp,-L)-\boldsymbol{z}_{\rm r}|L_{\rm r}L} \\ & \times \int_{\mathbb{R}^2} {\rm d}s_1 {\rm d}s_2 \exp\left[i\frac{\omega(L_{\rm r}-L)^2|(\boldsymbol{x}_\perp,-L)-\boldsymbol{z}_{\rm r}|}{2c_0 L_{\rm r} L}\left(s_1^2 \frac{(L_{\rm r}-L)^2}{|(\boldsymbol{x}_\perp,-L)-\boldsymbol{z}_{\rm r}|^2} + s_2^2\right)\right] \\ & \times \exp\left[-2i\frac{\omega}{c_0}\boldsymbol{z}\cdot\frac{(\boldsymbol{x}_\perp,-L)-\boldsymbol{z}_{\rm r}}{|(\boldsymbol{x}_\perp,-L)-\boldsymbol{z}_{\rm r}|}\right].\end{aligned}$$

We compute the integral in s_1 and s_2 and get the desired expression for $\mathcal{I}_{\rm I-}$. We carry out similar computations for $\mathcal{I}_{\rm I+}$, $\mathcal{I}_{\rm II-}$, and $\mathcal{I}_{\rm II+}$. Only $\mathcal{I}_{\rm II+}$ gives a nonvanishing contribution. In fact, we have $\mathcal{I}_{\rm II+} = \overline{\mathcal{I}_{\rm I-}}$. As a result, we obtain the expression (3.21) of the point spread function given in Proposition 3.3.

REFERENCES

[1] A. Bakulin and R. Calvert, *The virtual source method: Theory and case study*, Geophys., 71 (2006), pp. SI139–SI150.

[2] P. Blomgren, G. Papanicolaou, and H. Zhao, *Super-resolution in time-reversal acoustics*, J. Acoust. Soc. Amer., 111 (2002), pp. 230–248.

[3] L. Borcea, J. Garnier, G. Papanicolaou, and C. Tsogka, *Enhanced statistical stability in coherent interferometric imaging*, Inverse Problems, 27 (2011), 085004.

[4] L. Borcea, G. Papanicolaou, and C. Tsogka, *Theory and applications of time reversal and interferometric imaging*, Inverse Problems, 19 (2003), pp. S134–S164.

[5] L. Borcea, G. Papanicolaou, and C. Tsogka, *Interferometric array imaging in clutter*, Inverse Problems, 21 (2005), pp. 1419–1460.

[6] A. J. Calvert, *Ray-tracing based prediction and subtraction of water-layer multiples*, Geophys., 55 (1990), pp. 443–451.

[7] M. Cheney, *A mathematical tutorial on synthetic aperture radar*, SIAM Rev., 43 (2001), pp. 301–312.

[8] J. C. Curlander and R. N. McDonough, *Synthetic Aperture Radar*, Wiley, New York, 1991.

[9] A. Derode, E. Larose, M. Campillo, and M. Fink, *How to estimate the Green's function of a heterogeneous medium between two passive sensors? Application to acoustic waves*, Appl. Phys. Lett., 83 (2003), pp. 3054–3056.

[10] A. Derode, E. Larose, M. Tanter, J. de Rosny, A. Tourin, M. Campillo, and M. Fink, *Recovering the Green's function from field-field correlations in an open scattering medium*, J. Acoust. Soc. Amer., 113 (2003), pp. 2973–2976.
[11] A. Farina and H. Kuschel, *Guest editorial special issue on passive radar (Part I)*, IEEE Aerospace Electron. Syst. Mag., 27 (2012), issue 10.
[12] J.-P. Fouque, J. Garnier, G. Papanicolaou, and K. Sølna, *Wave Propagation and Time Reversal in Randomly Layered Media*, Springer, New York, 2007.
[13] J. Garnier and G. Papanicolaou, *Passive sensor imaging using cross correlations of noisy signals in a scattering medium*, SIAM J. Imaging Sci., 2 (2009), pp. 396–437.
[14] J. Garnier and G. Papanicolaou, *Correlation based virtual source imaging in strongly scattering media*, Inverse Problems, 28 (2012), 075002.
[15] J. Garnier and G. Papanicolaou, *Role of scattering in virtual source array imaging*, SIAM J. Imaging Sci., 7 (2014), pp. 1210–1236.
[16] J. Garnier, G. Papanicolaou, A. Semin, and C. Tsogka, *Signal to noise ratio analysis in virtual source array imaging*, SIAM J. Imaging Sci., 8 (2015), pp. 248–279.
[17] W. A. Kuperman and F. Ingenito, *Spatial correlation of surface generated noise in a stratified ocean*, J. Acoust. Soc. Amer., 67 (1980), pp. 1988–1996.
[18] E. Larose, L. Margerin, A. Derode, B. van Tiggelen, M. Campillo, N. Shapiro, A. Paul, L. Stehly, and M. Tanter, *Correlation of random wavefields: An interdisciplinary review*, Geophys., 71 (2006), pp. SI11–SI21.
[19] N. C. Makris, F. Ingenito, and W. A. Kuperman, *Detection of a submerged object insonified by surface noise in an ocean waveguide*, J. Acoust. Soc. Amer., 96 (1994), pp. 1703–1724.
[20] M. Rodriguez-Cassola, S. V. Baumgartner, G. Krieger, and A. Moreira, *Bistatic TerraSAR-X/F-SAR spaceborne-airborne SAR experiment: Description, data processing, and results*, IEEE Trans. Geosci. Remote Sens., 48 (2010), pp. 781–794.
[21] M. Rodriguez-Cassola, P. Prats, G. Krieger, and A. Moreira, *Efficient time-domain image formation with precise topography accommodation for general bistatic SAR configuration*, IEEE Trans. Aerospace Electron. Syst., 47 (2011), pp. 2949–2966.
[22] G. Papanicolaou, L. Ryzhik, and K. Sølna, *Statistical stability in time reversal*, SIAM J. Appl. Math., 64 (2004), pp. 1133–1155.
[23] P. Roux, W. A. Kuperman, and the NPAL Group, *Extracting coherent wave fronts from acoustic ambient noise in the ocean*, J. Acoust. Soc. Amer., 116 (2004), pp. 1995–2003.
[24] G. T. Schuster, *Seismic Interferometry*, Cambridge University Press, Cambridge, UK, 2009.
[25] M. Siderius, C. H. Harrison, and M. B. Porter, *A passive fathometer technique for imaging seabed layering using ambient noise*, J. Acoust. Soc. Amer., 120 (2006), pp. 1315–1323.
[26] K. Wapenaar, E. Slob, R. Snieder, and A. Curtis, *Tutorial on seismic interferometry: Part 2—Underlying theory and new advances*, Geophys., 75 (2010), pp. A211–A227.
[27] C. Yarman and B. Yazici, *Synthetic aperture hitchhiker imaging*, IEEE Trans. Imaging Process., 17 (2008), pp. 2156–2173.